
Experimental and Theoretical Analysis of Small-Scale Wind-Wave Generation

**PI's: G.R. Spedding, F.K. Browand & P. Newton
Department of Aerospace Engineering
University of Southern California
Los Angeles, CA 90089-1191**

DISTRIBUTION STATEMENT A

**Approved for public release
Distribution Unlimited**

Final Report on ONR Contract# N00014-92-J-1615

19971201 014

REPORT, DOCUMENTATION PAGE		Form Approved OMB No. 0704-0188	
Public reporting burden for this collection of information is estimated to average 1 hour per response, including the time for reviewing instructions, searching existing data sources gathering and maintaining the data needed, and completing and reviewing the collection of information. Send comments regarding this burden estimate or any other aspect of this collection of information, including suggestions for reducing this burden to Washington Headquarters Services, Directorate for Information Operations and Reports, 1215 Jefferson Davis Highway, Suite 1204, Arlington, VA 2202-4302, and to the Office of Management and Budget, Paperwork Reduction Project (0704-0188), Washington, DC 20503.			
1. AGENCY USE ONLY (Leave Blank)	2. REPORT DATE Aug. 4, 1997	3. REPORT TYPE AND DATES COVERED FINAL TECHNICAL REPORT 04/01/92 - 03/31/97	
4. TITLE AND SUBTITLE PROJECT TITLE Experimental and Theoretical Analysis of Small-Scale Wing Wave Generation		5 FUNDING NUMBERS CONTRACT NO. N00014-92-J-1615	
5. AUTHOR(S) Geoff Spedding, Paul Newton, Frederick Browand.			
7. PERFORMING ORGANIZATION NAME(S) AND ADDRESS(ES) UNIVERSITY OF SOUTHERN CALIFORNIA DEPARTMENT OF AEROSPACE ENGINEERING 854 W. 36 TH PL., RRB 101 LOS ANGELES, CA 90089-1191		8. PERFORMING ORGANIZATION REPORT NUMBER	
9. SPONSORING/MONITORING AGENCY NAME(S) AND ADDRESS(ES) Alan Brandt Office of Naval Research 800 N. Quincy St. Ballston Tower One Arlington, VA-22217		10. SPONSORING/MONITORING AGENCY REPORT NUMBER	
11. SUPPLEMENTARY NOTES			
12a. DISTRIBUTION/AVAILABILITY STATEMENT APPROVED FOR PUBLIC RELEASE; DISTRIBUTION UNLIMITED		12b. DISTRIBUTION CODE	
13. ABSTRACT (MINIMUM 200 WORDS) See enclosed.			
14. SUBJECT TERMS capillary gravity waves wavelet transforms		15. NUMBER OF PAGES 39 16. PRICE CODE	
17. SECURITY CLASSIFICATION OF REPORT UNCLASSIFIED	18. SECURITY CLASSIFICATION OF THIS PAGE UNCLASSIFIED	19. SECURITY CLASSIFICATION OF ABSTRACT UNCLASSIFIED	20. LIMITATION OF ABSTRACT UL

Abstract

This research project was initiated to explore the use of novel analysis techniques associated with emerging nonlinear methods to investigate the growth of capillary-gravity waves on an initially calm water surface following the abrupt start of wind forcing. During the course of the research, a novel wavelet-based method was devised and implemented for computing the local, instantaneous dispersion relation. The method is completely quantitative, and conserves energy. While averaged results showed exponential growth rates that agree approximately with linear theory, it is clear that details of the wave crest distribution that are important in determining subsequent nonlinear developments cannot be captured without not only a nonlinear theory, but also a 2D one. The most useful experiment to follow up this work would not be the obvious increase in scale, but would rather concentrate on a smaller scale facility where the 2D wind profile could be very closely controlled, and measured. Only then can the forcing effects be unambiguously separated from 2D nonlinear growth mechanisms.

Final Report on ONR Contract# N00014-92-J-1615

**PI's: G.R. Spedding, F.K. Browand & P. Newton
Department of Aerospace Engineering
University of Southern California
Los Angeles, CA 90089-1191**

Format of the report

Since the principal findings of the study have been published in two papers that are attached as appendices, the report itself will serve mainly to put these in overall context of the stated objectives, and to make some general conclusions from the two years work.

Original objectives

Initial wind energy input appears as small scale capillary gravity waves, whose evolution and transition to longer wavelengths is thus important in determining overall air-sea interaction energy budgets, and in generating surface roughness signatures that are detectable in SAR imagery. The original proposal promised to investigate the physical mechanisms of this process, using novel experimental and analytical techniques, combined with a theoretical analysis. The long-term goal is therefore (a) to improve basic physical understanding of small-scale wave generation mechanisms, (b) to make quantitative predictions of their rôle in ocean energy fluxes, and (c) to apply some of these concepts to remote sensing design and analysis.

Experimental and Theoretical Methods

These can be enumerated as follows:

1. The Imaging Slope Gauge (ISG) measurement technique, together with the Complex Wavelet Transform (CWT) dispersion relation analysis method was used to generate and test predictions for growth rates of capillary-gravity waves. The ISG method was adapted and refined in the first 3-year ONR-sponsored project. The CWT method was an entirely new method that came from the same effort. An extensive analysis was performed on data sets collected at the Air-Sea Interaction Research Laboratory, Wallops Island. Thorough, quantitative comparisons with results from numerical simulations of the nonlinear Schrödinger (NLS) equation have been conducted.
2. Theoretical models incorporating increasing degrees of realism (*i.e.* 3D/ unsteady/nonlinear effects) were developed, following indications from the results of #1 above. In particular, the theoretical analysis of Caponi *et al* (1992) was repeated, and a quasi-steady approximation allowed solutions to a time varying problem to be estimated by integrating over a boundary layer thickness that grows in time and has a profile according to experimental measurements.
3. Certain limits were identified in the application of current theoretical models and laboratory experiments in dealing with real problems of oceanographic and ONR relevance.

Brief summary of results

The results are given in more detail in the attached appendices, but the most important overall features can be summarised here.

1. *Experimental results* The initial wavenumbers and growth rates of the most unstable modes are well predicted by a linear instability of coupled water-air shear flow models. The initial wavenumbers are very close to theoretical predictions, but careful analysis of the growth rates, both from this study, and those in the literature, reveals that they are not predicted by the same degree of certainty. Factors of 2-4 difference are not uncommon. A new method of using the phase component of the CWT for automated recognition and tracking of defects has been developed. This 'waveprint' uniquely characterises a wave field in terms of its dislocation sites, or critical points, for a given wavenumber. A new method for estimation of friction velocities from a combined CWT/theoretical model has been developed.
2. *Theoretical models* The quasi-steady analysis shows that predicted dispersion relations are very sensitive to assumptions about the growth in characteristic scale of the air and water boundary layers. A simple viscous diffusion model completely fails to produce order of magnitude agreement with experiment. If the observed boundary layer growth is specified then the resulting dispersion relation differs from the free-wave problem in qualitatively similar ways to experimental data. It is clear that a more complex treatment is required. Some of the 3D structure in the surface deformation is due to defect patterns, and new, analytical, defect solutions to the NLS have been found.
3. *Limits* The current state of the theoretical art is found to be unsatisfactory. Existing linearised models that predict growth rates and mode amplitudes are very sensitive to extra inputs, such as boundary layer thickness and its time variation. Absent a predictive model of these data, even for controlled laboratory conditions, we lack a predictive understanding. The discrepancy with experimental data becomes more acute at higher wind speeds. The problem may indicate the inadequacy of the 2D (or 1D), linear model formulations. None of the latter stages of growth, where energy moves to increasingly lower wavenumbers, are satisfactorily modeled at present.
On the other hand, with current uncertainty in the exact form of the wind forcing, one cannot always separate the contributions from non uniformity in the wind forcing from genuine 3D instability modes. Paradoxically, further and deeper understanding of wave generation in ocean conditions may depend on the development of new, small-scale laboratory models, where the precise forcing can be known and varied.

Implications

Science/Physics: The current theoretical underpinnings of the wind wave initialisation problem have been shown to be less secure than previously thought, thanks to quantitative comparisons of unprecedented scope and accuracy. At the same time, the basic mechanism of air/water shear layer instability for initial wave generation is very solidly supported, and future theoretical developments must be based on this fundamental mechanism. The existing discrepancies indicate that either a 3D and/or a nonlinear model will be required for further progress.

Technology: CWT analysis has been used on both laboratory and ocean data now, since the instrumentation of the latter is improving. Technology is currently being shared between the two. The development of nonlinear mechanisms of wave growth occurs rapidly at all but the lowest wind speeds, and the development of the lower wavenumbers that persist in ocean applications is not yet modeled. The new friction velocity estimate has been developed specifically for field and SAR image data applications.

Collaborations and research transitions

The current project is a collaboration between USC (Spedding, Browand, Newton), NASA WFF (Huang, Long) and Scripps Institute of Oceanography (Jähne, Klinke). Internal NASA funds have been used to co-support much of this work. An AASERT studentship applying wavelet transforms to oceanographic measurements was spawned by this project and continues at USC. The collaboration with NASA Wallops was particularly successful, and we hope for further co-operative ventures.

Since the WT analysis has been developed and conducted on the dual SGI machines, purchased with NASA funds expressly for this purpose, the technique is transitioned very rapidly to the NASA government domain, and therefore, potentially, to application to large ONR- and NASA-sponsored databases. We have been active in ensuring that new programs are documented as they are written and NASA WFF has a complete, documented set of all software generated under this agreement.

Appendices

A. Spedding GR 1996 *2D Complex Wavelets for Analysis of Unsteady, Wind-Generated Surface Waves*. Nonlinear Dynamics of Ocean Waves. Special Issue of Naval Research Reviews, 58(3), 30-39.

B. Spedding GR, Klinke J & Long SR 1996 Estimating $\omega(k)$ in an unsteady, wind-generated surface wave field from the 2D complex wavelet transform of the surface slope. In: *The Air-Sea Interface: Radio and Acoustic Sensing, Turbulence and Wave Dynamics. Proc. Int. Symp. Marseille, 1993*. (eds M.A. Donelan, W.H. Hui & W.J. Plant), 373-382.

2D Complex Wavelets for Analysis of Unsteady, Wind-Generated Surface Waves

G.R.Spedding

Departments of Aerospace & Mechanical Engineering
University of Southern California
Los Angeles, CA 90089-1191

e-mail: geoff@ostrich.usc.edu

In: *The Nonlinear Dynamics of Ocean Waves*. Special issue of *Naval Research Reviews*, ed.
M Shlesinger 1996

Abstract

Wavelets and their transforms (WT) have numerous and diverse applications, and almost as many shapes and sizes. This article concentrates solely on their utility as a quantitative measure of spatially-localised spectral amplitudes for 2D data analysis. The physical problem concerns the time-dependent growth of wind-driven surface waves, starting from a flat surface. Although the problem lacks the full complexity of real ocean conditions, it is argued that because it is precisely defined, a combined experimental and theoretical program can advance our physical understanding, that may itself be projected onto field data. Certainly, the advent of nonlinearity in the wavefield is marked by intermittency and 3D structure, and the WT is an appropriate basis for analysis. The wind-wave problem will be used as an example where the simultaneous, quantitative measurement of amplitude and phase modulations in an unsteady wave field leads to estimates of quantities such as the local dispersion relation that cannot easily be measured otherwise. Furthermore, the WT-derived results can be combined with simple analytical models to measure quantities that are both of great interest to the oceanographer, and that have traditionally been difficult to estimate. Finally, suggestions are made for future work and take a surprising direction.

1. What is the problem?

Why study small-scale wind waves?

For the purposes of this article, small-scale waves are those having wavelengths in the centimeter range. Both gravitational and surface tension effects are significant and so the physical problem is an interesting balance between the two. From a practical point of view, there are two reasons for interest. Capillary-gravity (*cg*) waves are the wave-like disturbances that first grow when a calm water surface is disturbed by wind. Later in time, the energy-containing scales are much larger, but at any instant, it is through smaller-scale motions such as *cg* waves that the instantaneous surface response mediates the fluxes of momentum and energy between the atmosphere and ocean. The second practical motivation is that remote sensing devices such as SAR are sensitive to scattering of electromagnetic radiation primarily in the shorter wavelengths characterised by *cg* waves. It is only by modulation of the shorter wavelengths that larger scale features are observable. Generally it is sufficient to model this effect as a 'roughness', but statistical roughness models and predictions will not behave realistically unless they are based on sound physical principles. As we shall see later, the *cg* wavefield can be extremely complex in structure, and further understanding leads inevitably to studies that fall squarely into the 'Nonlinear Dynamics' theme of this issue.

Why study the unsteady problem?

It is a mild understatement to observe that fluctuations of the local wind stress (in both space and time) occur over the ocean surface. While steady-state response models may work satisfactorily in some statistical sense, the transient response and physical understanding of how one state changes to another, together with the possible interactions between a time-varying component with another stationary one, are still of great interest. Furthermore, while the linearised models predict the initial stages of the surface response quite well, they cannot predict the subsequent evolution of low wavenumber (long wavelength) modes, 3D pattern instabilities, and wave-wave interactions that follow. In other words, there still is a problem, and it has not yet been solved.

There is a second, more abstract, line of reasoning that also supports such a line of enquiry. One of the principal achievements of nonlinear dynamical systems theory has been to demonstrate how complex phenomena can be generated by simple, deterministic systems, with few degrees of freedom. Hopes have been raised that tasks of apparently daunting complexity may yet yield to analytical, predictive methods. In a similar vein, starting from

the very evident fact that the real sea surface state is extremely complicated, one searches for the simplest possible model that can nevertheless exhibit sufficiently rich dynamics that it can account for the most important physical mechanisms.

Starting from scratch, we require a system that: (i) is clearly defined; (ii) can be modeled analytically, or numerically; (iii) can be tested experimentally, and (iv) can be generalised to situations of practical interest. Condition (iv) is rarely satisfied unless (ii) and (iii) involve a degree of understanding based on physical principles, and the failure of empirical matching of model parameters and coefficients when applied outside of the domain for which they have been carefully tuned is a rather familiar problem in oceanography.

The spectrum of analytical models for the air-water interface is bounded on the one hand by small amplitude, two-dimensional solutions of the Rayleigh equation for steady mean flows with boundaries at $x = \pm\infty$. Correspondingly, the Blasius solution to the incompressible, flat-plate boundary-layer equations for a specified origin in x gives the fetch-limited result. Between the two limiting cases, we are interested in the time-dependent problem, in the absence of external boundaries.

One might question the relevance of laminar model flows when the ocean applications are almost always turbulent, in both fluids. However, in the initial transient for a wind profile starting from rest, even if the flow itself is not perfectly laminar, the laminar instability modes could still be predominant in selecting the most energetic wave modes. In this respect, the laboratory experiment, incorporating some degree of turbulence in the growing profiles, provides a bridge between model and reality.

Why bother with laboratory experiments?

In the previous article, Norden Huang has considered the general applicability of wave-tank experiments to real ocean conditions. It is worth reiterating the basic philosophy behind our laboratory work and its relation to the overall problem outlined in the previous paragraphs. In contrast to field data, it is only in the relatively controlled conditions of the laboratory that parameters can be varied at will, independently, and repeatedly. It is not necessarily significant that conditions do not exactly match those of the open ocean, because the experiments can still provide non-trivial tests of analytical or conceptual models that are themselves of use over a broader range of parameters. The support or refutation of such models can still provide information about their ability to predict events in the real world. If and when the model fails, it can be extended or thrown away; in either event, the conditions under which it fails are now known.

In the remainder of this article, a closely-linked theoretical and experimental research program will be described, where wavelet analysis will be used as a tool for identifying current limitations and pointing to future requirements.

2. The contribution of wavelet-based methods

Wavelets as atomic units

At the time of writing, there are 11 texts on wavelets in our university bookstore, and some are quite good. For a concise and readable introduction, it is hard to beat the *Algorithms and Applications* book by Meyer¹. A more comprehensive and mathematical overview is presented in the introductory volume of the series on wavelets edited by Chui², and geophysical applications of varying quality can be found in a later volume³ in the same series. Farge⁴ has written a fine review on wavelets and turbulence, and further collections of theoretical advances and applications are accumulating.^{5,7}

One of the great strengths of the field is in the mathematical depth and rigour of much of the derivation and analysis, which has revealed connections with hitherto unrelated techniques, from Littlewood-Paley analysis of the 1930's to modern quadrature mirror signal processing

algorithms and spline functional analysis. Nevertheless, a zero-th order degree of sophistication in understanding wavelet-based signal analysis will suffice for our purposes. On this level, wavelets are simple oscillatory functions that have compact support, and thus can be used for local space-scale decompositions. The original function, $f(x)$ (or $f(t)$), is expanded as a function of an additional scale variable, a

$$f(x) \rightarrow \tilde{f}(a, x). \quad (1)$$

The decomposition is effected by a convolution of $f(x)$ with multiple copies of a single wavelet function, $\psi(x)$, that are systematically shifted and dilated to cover a range of characteristic scales, a , and positions, b .

Provided certain admissibility criteria are met ($\psi(x)$ must have finite energy, zero mean...consult refs.(1,2,4)), then the choice of $\psi(x)$ is somewhat arbitrary. It is possible to make the strong assertion that the physical world is much more likely to be composed of collections of wavelet-type, compactly supported functions, rather than, say, infinitely-extended oscillatory functions as in Fourier series. It follows that it is only reasonable to decompose real world observations (and computations) onto such atomic units. Farge⁴, for example, draws attention to the fact that a decomposition of a complex fluid flow into its elementary coherent structures (if such an object exists), is better approximated by a functional base with compact support than the usual Fourier base. Alternatively, one might search for basis functions whose properties are extracted from the data, or from known solutions to the particular governing equations. There will likely be future progress in this direction, but it is in fact unnecessary to adhere so strictly to the atomic construct.

Wavelets as tools for quantitative description

The keyword, of course, is 'construct', and one is free to construct a wavelet, or any other, basis to represent the world in many different ways. For example, one of the principal advantages of Fourier representations is the considerable mathematical convenience in computation of PDE's, having little or nothing to do with any implied physical basis. Similarly, provided one is aware of the properties of the decomposition and its rôle in determining (even distorting) the interpretation of the world, one can still use a wavelet basis for descriptive purposes. This is not all the same thing as stating that wavelet-atoms actually exist, or that they have any special dynamical significance. Hence, we simply state the following:

1. *The objective is to make quantitative measurements and interpretations of local energy densities in a 2D, time-varying surface wave field.*
2. *The most straightforward way to do this is through continuous, complex-valued wavelets.*

The definition of the wavelet transform (WT), described in words above, can be stated more precisely:

$$\tilde{f}(a, b) = \int f(x) \cdot \psi^* \left(\frac{x-b}{a} \right) dx. \quad (2)$$

The transform is a sum of the convolution of the translates and dilates of $\psi^*(x)$ with $f(x)$ (the * denotes the complex conjugate). In one dimension, a useful choice of $\psi(x)$ is the Morlet⁵ wavelet

$$\psi(x) = e^{ik_0 x} \cdot e^{-(1/2)(x^2/\lambda^2)}. \quad (3)$$

As Figure 1 demonstrates, it is a complex-valued function, and the $\pi/2$ phase shift between real and imaginary parts allows the modulus of its coefficients to be free from oscillations due to changes in phase in an otherwise constant amplitude signal. The wavelet phase indicates the phase in the instantaneous frequency, or wavenumber, associated with a particular scale, a .

k_0 is constant (typically $k_0 \in]5.5, 6[$) so there is a fixed number of cycles in an analysing wavelet, regardless of a . Consequently, the spatial resolution improves with increasing wavenumber, or decreasing a . The way in which it does so varies automatically with a , and the balance between resolution in wavenumber space and in physical space is in some sense an optimum for the Morlet wavelet, within the overall constraints of Heisenberg's uncertainty principle.

The WT conserves energy, and a form of the Parseval relation can be written,

$$\int_{-\infty}^{\infty} |f(x)|^2 dx = \frac{1}{C_\psi} \int_0^{\infty} \int_{-\infty}^{\infty} |\tilde{f}(a,b)| \cdot |\tilde{f}^*(a,b)| \frac{dadb}{a^2}, \quad (4)$$

where C_ψ is a normalisation constant that depends on the form of $\psi(x)$. The right hand side is an integral of a function that is proportional to the spatial distribution of energy density per unit scale. It is possible to integrate contributions from all x to arrive at a global power spectrum,

$$E(a) = \frac{1}{C_\psi} \int_{-\infty}^{\infty} |\tilde{f}(a,b)|^2 \frac{db}{a^2}. \quad (5)$$

$E(a)$ is a Gaussian-smoothed version of a power spectrum that could equally well have been obtained from Fourier transforms. Of course, in this case we are not obliged to perform the summation over x , and the point is to note that the energy densities are precise, quantitative measures of localised spectral components (provided that there are no artifacts from the mutual interaction of overlapping, non-orthogonal wavelet coefficients).

The extension to two dimensions of this basic approach is fairly straightforward and details can be found in ref. 9. As before, we require a complex wavelet function, and for real-valued signals (2D surface slope measurements, for example) it is sufficient to cover the half-plane in wavenumber space. Now that $\psi = \psi(x,y)$, the wavelet can be designed so that it can be either directional-specific, or non-directional. A non-directional wavelet responds equally to wavevectors at all angular orientations, and in two dimensions such a function covers an arc that sweeps through 180° in $\{k_x, k_y\}$ (Fig. 2).

Arc and its close relatives form the core of the data analysis, giving a measure of instantaneous, wavenumber energy densities and wave phase as a function of $\{x,y\}$.

3. An integrated analytical/experimental program

Theory

The time-varying solution for perturbations to the interface between two viscous fluids with specified shear-flow profiles can be solved numerically by integrating coupled Orr-Sommerfeld equations for air and water. Both Valenzuela¹⁰ and Kawai¹¹ have done that, two decades or so ago. Exponential growth rates for *cg* waves were predicted (and measured, in the case of Kawai) and compared reasonably well with microwave backscatter measurements of Larson & Wright.¹² This body of work represents, still, the state-of-the-art in the numerical analysis of the linearised problem.

The stability of piecewise linear shear profiles in air and water was recently examined by Caponi *et al.*¹³ One can take their steady-state model and integrate forwards in time by allowing a boundary layer thickness to grow, thus generating a quasi-steady solution. The sensitivity of the solution to the assumed growth of the boundary layer thickness will tell us

much about the behaviour of the numerical solutions, and the directions for further improvements.

Experiment

Experimentally, we investigate the growth of disturbances on an initially calm water surface when the wind starts from rest, and at sufficient fetch so that upstream boundary conditions can be ignored (at least in the water). The configuration is a reasonably close experimental approximation of the theoretical approaches discussed above.

The measurements are made with a modified form of the Imaging Slope Gauge (originally described by Jähne & Riemer¹⁴), which uses surface refraction of intensity-graduated incident light to derive the instantaneous along- or cross-wind slope over the field of view. $s_x(x,y,t)$ or $s_y(x,y,t)$ can be reconstructed according to the direction of the light intensity gradient. The surface slope, s_x , is directly related to the wave energy, and the WT time series, $s_{xy}(x,y,a,t)$ contains information about the local energy densities, and about the local wavenumber-frequency relation. Model predictions can thus be carefully checked. For the first time, the unsteady, local dispersion relation can be measured, and related to the 2D, instantaneous structure of the wavefield.

Matching the two

Neither existing models, nor practicable experiments can provide complete and generalisable information about the time-varying, 3D, wave and velocity fields. It will emerge that the theoretical models are very sensitive to, and experiments mostly ignorant of, the detailed shape and time-evolution of the water and air boundary layers. However, in combination, mutual consistency checks and judicious matching of empirical data with analytical relations can lead to new methods for measuring and/or inferring the values of physical variables (surface stress, boundary layer height), not only from laboratory data, but also from remote sensing measurements. Two examples of this kind of reasoning will be given. In both cases, the glue that holds the pieces together is the *Arc* wavelet transform.

4. The time evolution of capillary-gravity waves

The surface wave growth for a mean wind, $U_{10} = 6.8$ m/s (measured at 10 cm above the calm water surface) is shown in Figure 3. The time series proceeds from left to right, top to bottom, and is for wind forcing from the right. The dimensionless time $\tau = U_{10}t/X$, where X is the fetch, ranges from 3 to 5.5, so the upstream origin is always felt in the air flow, even at the early times. The group velocity of the initial water waves, however, is much smaller. At 50 cm/s, for example, 24 seconds are required to travel the fetch distance of 12m.

It is clear that, even at early times, the observed wavefield is never perfectly two-dimensional. The grey-scale encoding of the slope magnitude gives the initial disturbances an organ-pipe appearance, but they always have Y-shaped 'defects', or 'dislocations', where successive waves become entangled. In fact, it was the presence of the defect patterns that first drew our attention to the wind-wave problem, as we wondered whether there may be similarities with other defect structures in fluid turbulence.¹⁵⁻¹⁷

Even though the waves are not perfectly two-dimensional, calculation of the global power spectral densities and their rate of change with time shows that the most amplified wavenumbers, and their initial exponential growth rates, can be quite well predicted by linear theory (Figure 4). That is true for the first five images (the top row) in Figure 3. During the course of about 1.25s, the initially most-amplified disturbances have reached their maximum amplitude, and in the top right panel, the waves look as two-dimensional as they ever will be. Shortly afterwards, the surface patterns become much more complicated as the initial modes saturate and further growth occurs in sidebands of both higher and lower wavenumber. By the end of the series longer wavelength disturbances predominate. A convincing physical explanation for this well-known phenomenon has never been given. Note, however, that it

does appear to be a duration-limited event, since information propagated by water waves from upstream boundaries will not yet have reached the measurement window. Further insights can be derived from wavelet analysis.

5. Wavelet-based analysis

Local energy density distributions

The remarks concerning the global evolution of instability modes are based on Fourier analysis. The 2D Fourier transform can provide a perfectly good description of the average properties of the surface slope, and has very good spectral resolution. Having identified the wavenumbers of interest, it is now possible to use the localised properties of the wavelet transform to relate the spectral densities to the structure of the wavefield.

The spatial distribution of growth of the initially most amplified mode at $U_{10} = 6.8$ m/s can be seen in Figure 5. The energy density distributions are quite patchy, and remain so. By analogy with defects in mixing layers, where the defects are the sites for the first (and subsequent) subharmonic transitions, it is reasonable to ask whether the globally-measurable sideband instabilities are located at, or near, defect sites in the surface wave field. The open circles denote the location of defects, identified by eye in the equivalent time series of surface slope. Again, by analogy with the mixing layer results, the local energy density at the fundamental scale, a_0 , would be a minimum here, while the sideband modes would peak at the same location. At first glance, the circles do seem to be consistently beside, rather than on, the highest energy densities in a_0 . However, Figure 6, which is the same plot for the lower wavenumber sideband, a_{-1} , shows that the circles are *not* associated with local maxima at this scale. It can also be found that the other sideband, characterised by wavelet scales a_1 , is correlated quite well with maxima in a_{-1} , and so, also not with a_0 . The high and low wavenumber modes correlate well with each other, but only weakly with minima in the initial mode. Initially, the defects do not appear to play a significant rôle in the development of sidebands. Although one cannot expect spatial correlations to be maintained in a dispersive wavefield, the variation in phase speed with wavenumber is rather weak at this particular range of scales, and the wave pattern defects or dislocations do not appear to be involved in the growth of sidebands.

Pattern defects and the waveprint

The correlation of pattern defects with various postulated transitions and instabilities could be made more precise if a reliable method for identifying the defect sites were available, and we recently found one.

Recall that it is specifically defects at a particular scale that we would like to investigate, and the WT can be employed as a kind of filter so that only contributions from this scale are counted. Images such as Figures 5 & 6 are clearly of no use, but the phase of the WT is. Figure 7 is a binarised image of the phase of the WT at scale a_0 . Not only can one confirm the defect locations that were originally identified by eye (circles), but it is also possible to follow their time evolution. None of the defect topologies in the circles remains fixed over time; instead connections with preceding or following waves are initiated and broken. In a similar spirit to the description of fluid flows by critical points,¹⁸ the wavefield topology can be characterised by the type and location of its defects, together with the distribution of the highest amplitude wavelet coefficients. Just as fingerprints can be categorised by their defects, so the wavefield can be described by its waveprint. One can look for particular defect structures in an appropriate analytical model, and Paul Newton at USC has made a start in describing a new family of defect solutions to the nonlinear Schrödinger equation.¹⁹

6. Combined analytical/experimental models for prediction

Estimation of local dispersion relation

The WT gives a measure of the spatially-localised energy densities as a function of wavenumber, and since the measurements are also well-resolved in time, the local frequencies can be calculated from $\omega = \partial\phi/\partial t$. This is possible because the complex WT also gives the instantaneous phase distribution, $\phi(x,y)$, associated with each scale (as shown in the waveprint). Figure 8 shows how the calculation proceeds. The flowfield, $u(x,y)$, that maps $\phi(x,y,t_1)$ to $\phi(x,y,t_2)$ at all energetic scales, a (associated with physical wavenumber, k), is used to compute the local frequency as

$$\bar{\omega}(x,y) = |k(x,y)| \bar{u}(x,y). \quad (6)$$

There is no comparable time-dependent, 2D theory that predicts such a detailed dispersion relation, but values over all $\{x,y\}$ can be collected together and compared. Figure 9 is an example, where the solid curves have been drawn over an arbitrary range of k from the result of Caponi *et al*¹³ for the intrinsic $\omega(k)$ of small perturbations on a surface between two piecewise linear shear profiles. The experimental results differ from the theoretical curves, which is not altogether surprising since the wavelengths (and frequencies) that actually have the largest amplification rate in practice will depend on the time history of the growth in boundary layer thickness, $D(t)$, and surface drift velocity, $U_w(t)$. In fact, from the difference between the measured $\omega(k)$ and the solid curve, either the surface drift or the boundary layer thickness can be inferred. This is an example of a combined experimental/theoretical modeling for simultaneous measurement of a variable whose estimation could be of great importance in the field.

Estimation of surface stress from lab. or field data

Now let us suppose that U_w is known (from existing experimental data or field measurements. The maximum slope thickness, D , can be written as the ratio of the mean wind, U , to the gradient of $\partial U/\partial y$ at the water surface

$$D = \frac{U}{\left. \frac{\partial U}{\partial y} \right|_{y=0}}. \quad (7)$$

The friction velocity, u_* , is a measure of the wind stress exerted at the water surface, which also varies with $\partial U/\partial y$:

$$u_*^2 = \frac{\tau_{y=0}}{\rho} = \frac{\mu}{\rho} \left. \frac{\partial U}{\partial y} \right|_{y=0}. \quad (8)$$

where μ and ρ are the air viscosity and density, respectively. Combining the two expressions, the friction velocity can be related to D ,

$$u_*^2 = \frac{\nu U}{D}, \quad (9)$$

where $\nu = \mu/\rho$ is the kinematic viscosity. An estimate of D is therefore equivalent to an estimate of the friction velocity. To see how this relationship can be incorporated into the overall framework, see Figure 10. At the heart of the scheme is the combined theoretical model for $\omega(k)$ together with experimental measurements of the same quantity. Given a measured dispersion relation, and a selection criterion for choosing one particular curve, such as the

maximum amplification rate, then the difference between measured and predicted $\omega(k)$ curves can be attributed to the surface drift current, U_w . The corrected ratio of the water and air velocities are returned to the theoretical model, and upon convergence, a predicted value of $D=D_p$ can be used to measure u_w . It is noteworthy that the measurements do not have to come from laboratory data. In principle, a time series of SAR images could provide the same information, because the WT can give estimates of $\omega(k)$ from these data also.

The two examples above demonstrate how the newly-acquired ability to measure instantaneous amplitude and phase information for local spectral components can lead to novel and potentially powerful measurement techniques that have application in both laboratory and ocean data.

7. Concluding remarks

The wind-wave startup problem has been explored as an example of the application of wavelet-based measurement and analysis techniques to unsteady, inhomogeneous data. It is the extension to these domains that brings us closer to realistic ocean conditions, and clearly into nonlinear regimes that have just begun to be investigated. The advanced measurement techniques have application to both laboratory and field conditions.

With regard to the particular wind-wave problem, it is obvious that the wavefield is always quite complex in structure, but the dynamical significance of the complexity is not equally obvious. In attempting to distinguish between structure that is due to intrinsic instability of the water surface deformation, or that merely reflects imprecision in specification of the initial forcing, we need a smaller-scale, more easily controllable experiment. The form of the mean wind profile, and its time history, must be specified. Then, an experimental program with modulations in both along- and cross-wind directions to generate particular instability modes would be a wind-forced equivalent of existing systematic investigations of liquid surface instabilities.²⁰⁻²³

Paradoxically, the conclusion that future experiments ought to be in smaller, more precisely-controlled containers, moves still further from true-blue oceanography, where Reynolds numbers are large, and many simultaneous processes compete and/or interact with each other. Recalling the introduction however, it is likely that the basic instabilities and physical mechanisms will only be isolated and identified with a more selective, and precisely specified experiment. We hope to report on the results of similar experiments in the future.

Acknowledgments

It is a pleasure to thank my friends and colleagues, Paul Newton, and especially, Fred Browand, for their expert counsel during the course of this research. We thank also our co-collaborators Norden Huang and Steve Long, at NASA Goddard/Wallops Island, and Bernd Jähne and Jochen Klinka at Scripps Institute. All of us thank Lou Goodman and Mike Shlesinger for their support, and also Alan Brandt, who helped initiate the research while he was at ONR.

References

- 1 Meyer Y 1993 *Wavelets: Algorithms and Applications*. SIAM, Philadelphia
- 2 Chui CK 1992 *Wavelet Analysis and its Applications*. (ed. CK Chui) Volume 1: *An Introduction to Wavelets*. Academic Press, New York.

- 3 Geogiou EF & Kumar P 1994 Wavelet Analysis and its Applications. (ed. CK Chui) Volume 4: *Wavelets in Geophysics*. Academic Press, New York.
- 4 Farge M 1992 Wavelet transforms and their applications to turbulence. *Ann. Rev. Fluid Mech.* **24**, 395-457.
- 5 Ruskai M, Beylkin G, Coifman R, Daubechies I, Mallat S, Meyer Y & Raphael L 1992 *Wavelets and their Applications*. Jones & Bartlett, Boston.
- 6 Benedetto JJ & Frazier MW 1994 *Wavelets: Mathematics and Applications*. CRC Press, London.
- 7 Chui CK, Montefusco L & Puccio L 1994 Wavelet Analysis and its Applications. (ed. CK Chui) Volume 5. Academic Press, New York.
- 8 Grossmann A & Morlet J 1984 Decomposition of Hardy functions into square integrable wavelets of constant shape. *SIAM J. Math. Anal.* **15**, 723-736.
- 9 Dallard T & Spedding GR 1993 2D wavelet transforms: generalisation of the Hardy space and application to experimental studies. *Eur. J. Mech. B/Fluids* **12**, 107-134.
- 10 Valenzuela GR 1976 The growth of gravity-capillary waves in a coupled shear flow. *J. Fluid Mech.* **76**, 229-250.
- 11 Kawai S 1979 Generation of initial wavelets by instability of a coupled shear flow and their evolution to wind waves. *J. Fluid Mech.* **93**, 661-703.
- 12 Larson TR & Wright JW 1975 Wind-generated gravity-capillary waves: laboratory measurements of temporal growth rates using microwave backscatter. *J. Fluid Mech.* **70**, 417-436.
- 13 Caponi EA, Caponi MZ, Saffman PG & Yuen HC 1992 A simple model for the effect of water shear on the generation of waves by wind. *Proc. R. Soc. Lond. A* **438**, 95-101.
- 14 Jähne B & Riemer KS 1990 Two-dimensional wave number spectra of small-scale water surface waves. *J. Geophys. Res.* **95**, 11531-11546.
- 15 Dallard T & Browand FK 1993 The growth of large scales at defect sites in the plane mixing layer. *J. Fluid Mech.* **247**, 339-368.
- 16 Couillet P, Gil L & Lega J 1989 A form of turbulence associated with defects. *Physica D* **37**, 91-103.
- 17 Spedding GR, Browand FK, Huang NE & Long SR 1993 A 2D complex wavelet analysis of an unsteady wind-generated surface wave field. *Dy. Atmos. Ocean* **20**, 55-77.
- 18 Perry AE, Lim TT & Chong MS 1980 The instantaneous velocity fields of coherent structures in coflowing jets and wakes. *J. Fluid Mech.* **101**, 243-256.
- 19 Newton PK & O'Connor M 1996 Scaling Laws at Nonlinear Schrödinger Defect Sites. *Phys. Rev. E*. (to appear)
- 20 Henderson D & Hammack J 1987 Experiments on ripple instabilities. Part 1. Resonant triads. *J. Fluid Mech.* **184**, 15-41.
- 21 Perlin M, Henderson D & Hammack J 1990 Experiments on ripple instabilities. Part 2. Selective amplification of resonant triads. *J. Fluid Mech.* **219**, 51-80.
- 22 Perlin M & Hammack J 1991 Experiments on ripple instabilities. Part 3. Resonant quartets of the Benjamin-Feir type. *J. Fluid Mech.* **229**, 229-268.
- 23 Liu J, Schneider JB & Gollub JP 1995 Three-dimensional instabilities of film flows. *Phys Fluids* **7**, 55-67.

Figure captions

Figure 1 Is the world composed of wavepackets like this? The Morlet wavelet is a smooth, continuous wave function, modulated by a Gaussian envelope. Real and imaginary parts are shown in continuous and dotted lines. Whether or not it is a true atomic unit of the physical world, it can still be a convenient function basis for general description.

Figure 2 The 2D wavelet function *Arc* is defined most conveniently in Fourier space where for a given scale, a , it can be seen to interrogate an arc that covers all wavevectors of magnitude $|k|$, regardless of their orientation.

Figure 3 The time evolution of alongwind surface slope following a change in mean wind, U_{10} , from 0 m/s to 6.8 m/s. The change in wind speed is approximately linear over 5 seconds. The time series shown here begins at $t=5.3s$, i.e. after U_{10} has reached its steady value. The field of view in each image is approximately 14×11.5 cm.

Figure 4 Experimentally-measured initial exponential growth rate, β , vs. wavenumber, k_x (symbols connected by solid lines), for U_{10} from 2.8 - 10.2 m/s. The solid symbols are from experiments of Kawai, and the dashed lines are results from Kawai's Orr-Sommerfeld model integration for parameters that closely matched those experiments (U_{10} is given in brackets). At moderate windspeeds, the agreement is good, but is very sensitive to assumptions about how the boundary layer grows, and so remains somewhat empirical, because there is no analytical model for the boundary layer growth. A simple diffusion model does not work at all, and a pessimist might well argue that the agreement simply signifies that both parties have done similar experiments. As selected, the best match occurs at moderate windspeeds, but the extremes are not so well covered.

Figure 5 The modulus of the wavelet transform, $|WT|_{a_0}$, at the initially most amplified scale ($k_0=4.0$ rad/cm, $\lambda_0=1.6$ cm). The colour bar mapping is constant over the series, which covers the exponential growth, saturation, and decline in energy densities around this scale. Although the wavenumber and growth rates are quite well predicted, as described in Figure 4, the distribution is far from uniform in $\{x,y\}$.

Figure 6 $|WT|_{a_1}$ for same time series as Figure 5. Maximum growth of the lower wavenumber mode ($k_1=2.2$ rad/cm, $\lambda_1=2.9$ cm) occurs around the middle of the third row, just when the peak of the initially most amplified mode in Figure 5 begins to saturate and decay. The boxes marked ' k_1 ' are located at the energy density peaks and correlate well with peaks at the higher wavenumber mode ($k_1=7.9$ rad/cm, $\lambda_0=0.8$ cm; not shown).

Figure 7 The waveprint. The sign of the phase of the WT at a_0 allows defect sites to be located with little ambiguity, enabling automated identification and tracking algorithms to work reliably.

Figure 8 How to calculate the instantaneous, local dispersion relation $\omega(k, x, y)$ from a time series of complex wavelet transforms. Given the surface slope distribution, $s_f(x,y)$ (top row), at two closely-spaced times, t_1, t_2 , the wavelet transform of each can be separated into modulus and phase components (rows 2 & 3). For all scales having significant energy densities, the flow field that maps the isophase lines from their position at t_1 to their position at t_2 can be computed from an optical flow technique. Note that frequencies higher than the apparent Nyquist limit can be found because the structure in the phase field allows large displacements to be computed in a global optimisation solution. Finally, only measurements that occur where $|WT| > |WT|_{\text{thresh}}$ are retained.

Figure 9 An example comparison of measured $\omega(k)$ with theoretical predictions in solid curves. Each symbol marks the average value of the collection of points at a particular wavenumber where $|WT|$ exceeds a threshold value. Each spatial location contributes a dot,

and the collection of dots forms a vertical line whose length shows the variation in measured ω for a given k . The first two timesteps cover the regime that is adequately described by linear theory. After $\tau=4.95$, the scatter increases and by $\tau=5.23$, there are no wavelet coefficients that exceed the threshold value at the originally most-amplified wavenumber.

Figure 10 A flow diagram for the procedure for estimating wind friction velocity from measured inputs, ω , k and U_* . The inputs may come from either laboratory or field data. The subscripts w and a refer to quantities in water and air, respectively, and subscripts m and p identify measured and predicted values.

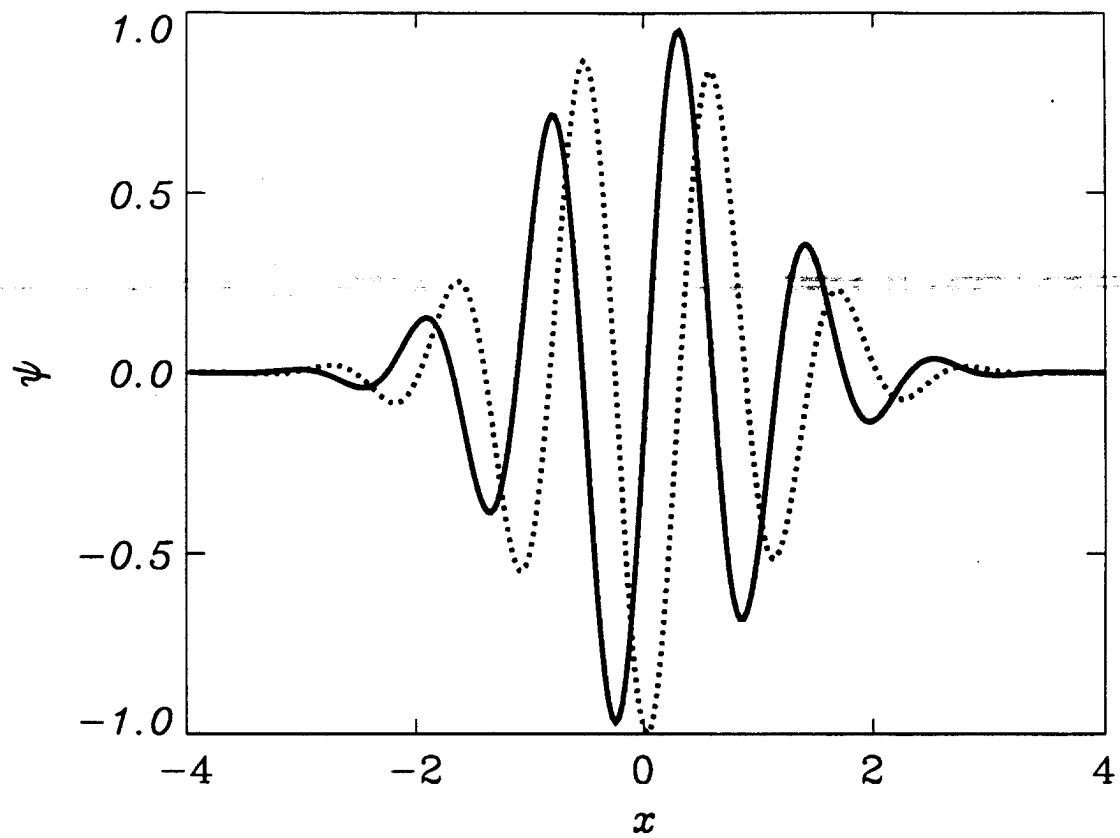


Fig. 1

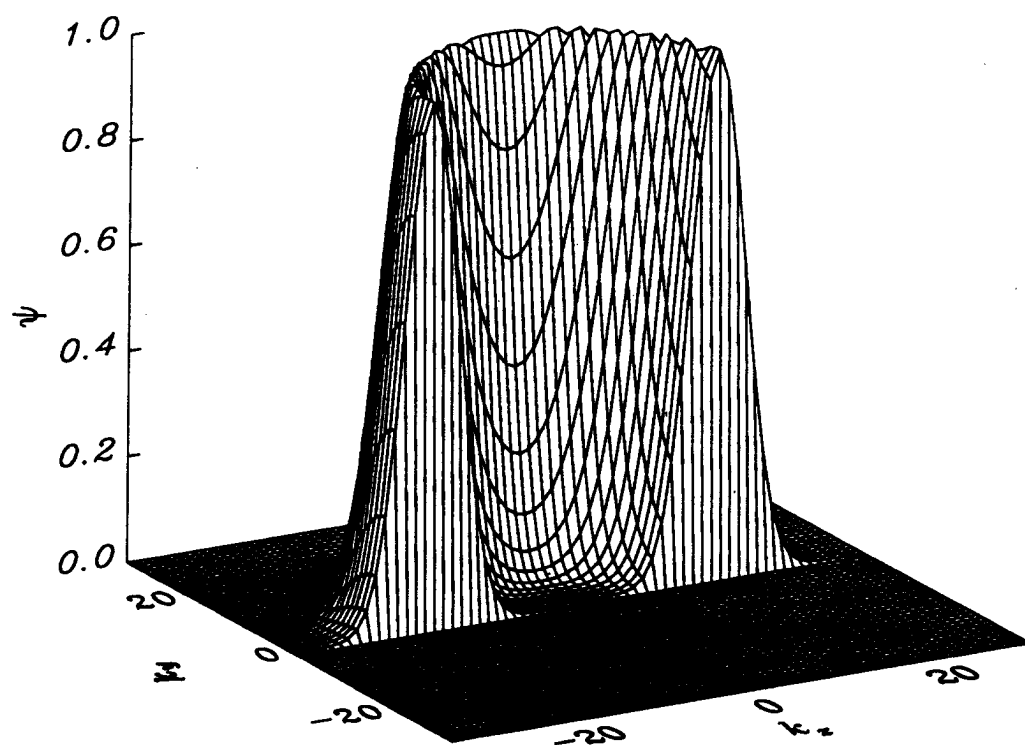
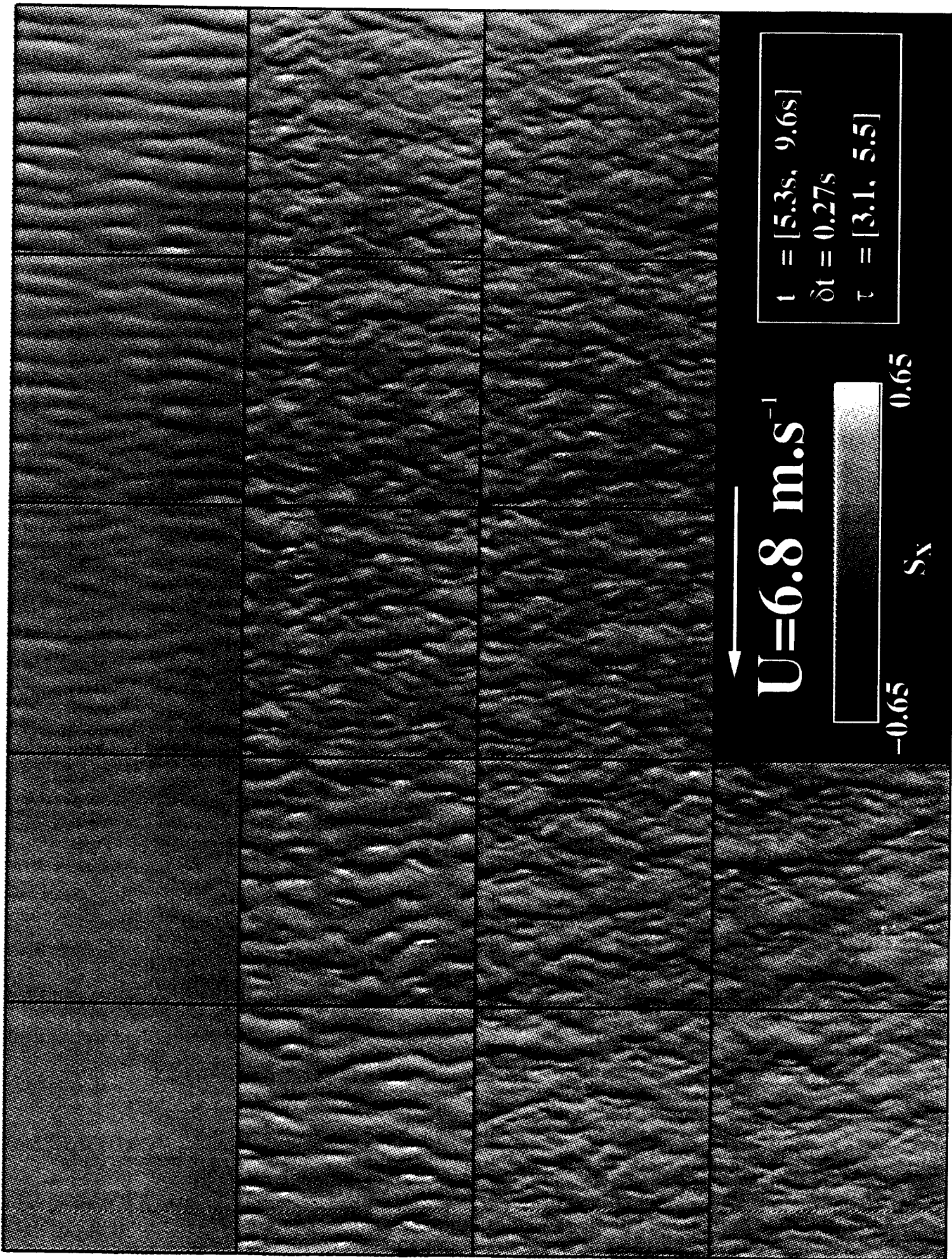


Fig. 2



$U=6.8 \text{ m.s}^{-1}$



-0.65

0.65

S_x

$t = [5.3s, 9.6s]$
 $\delta t = 0.27s$
 $\tau = [3.1, 5.5]$

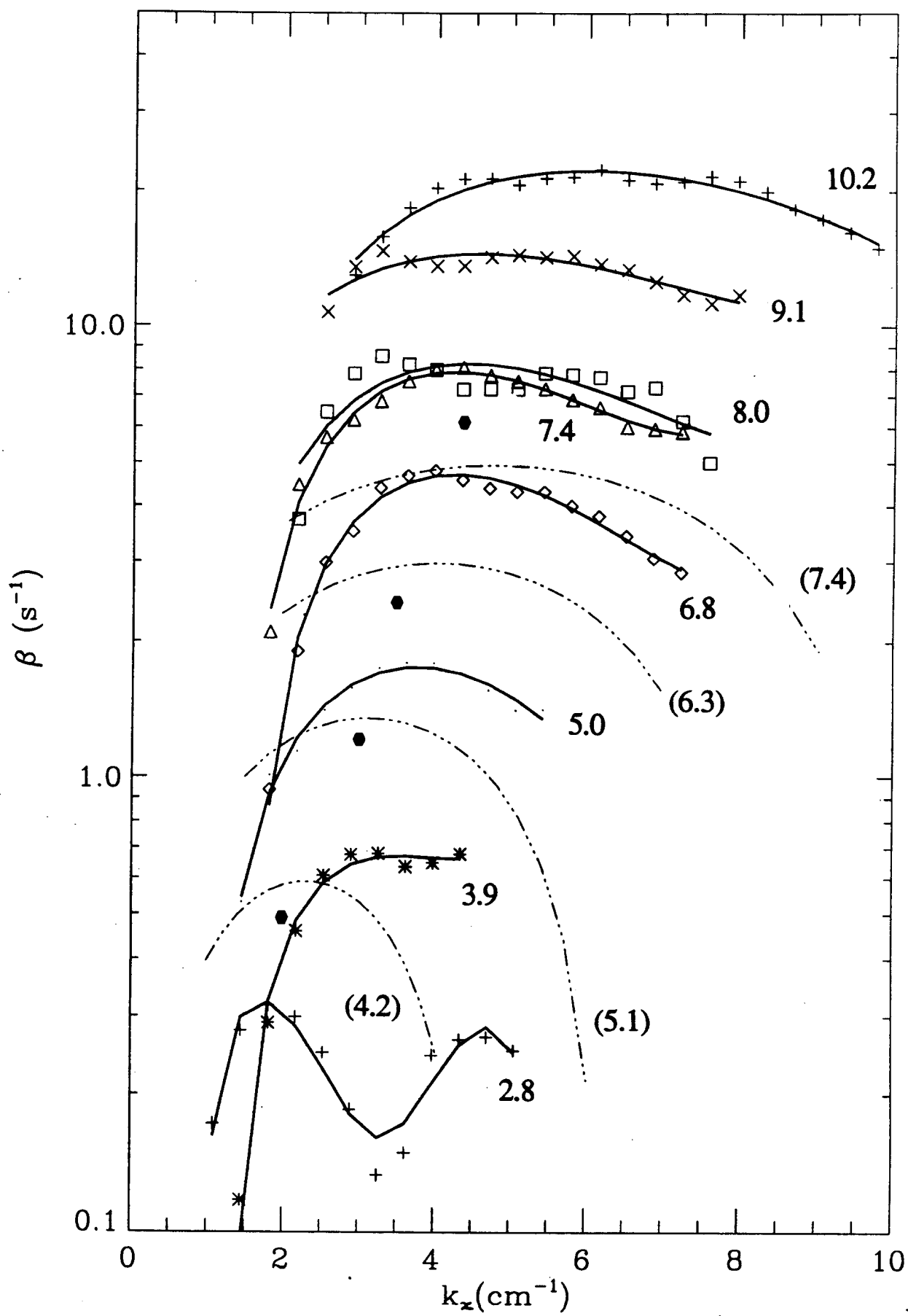


Fig. 4

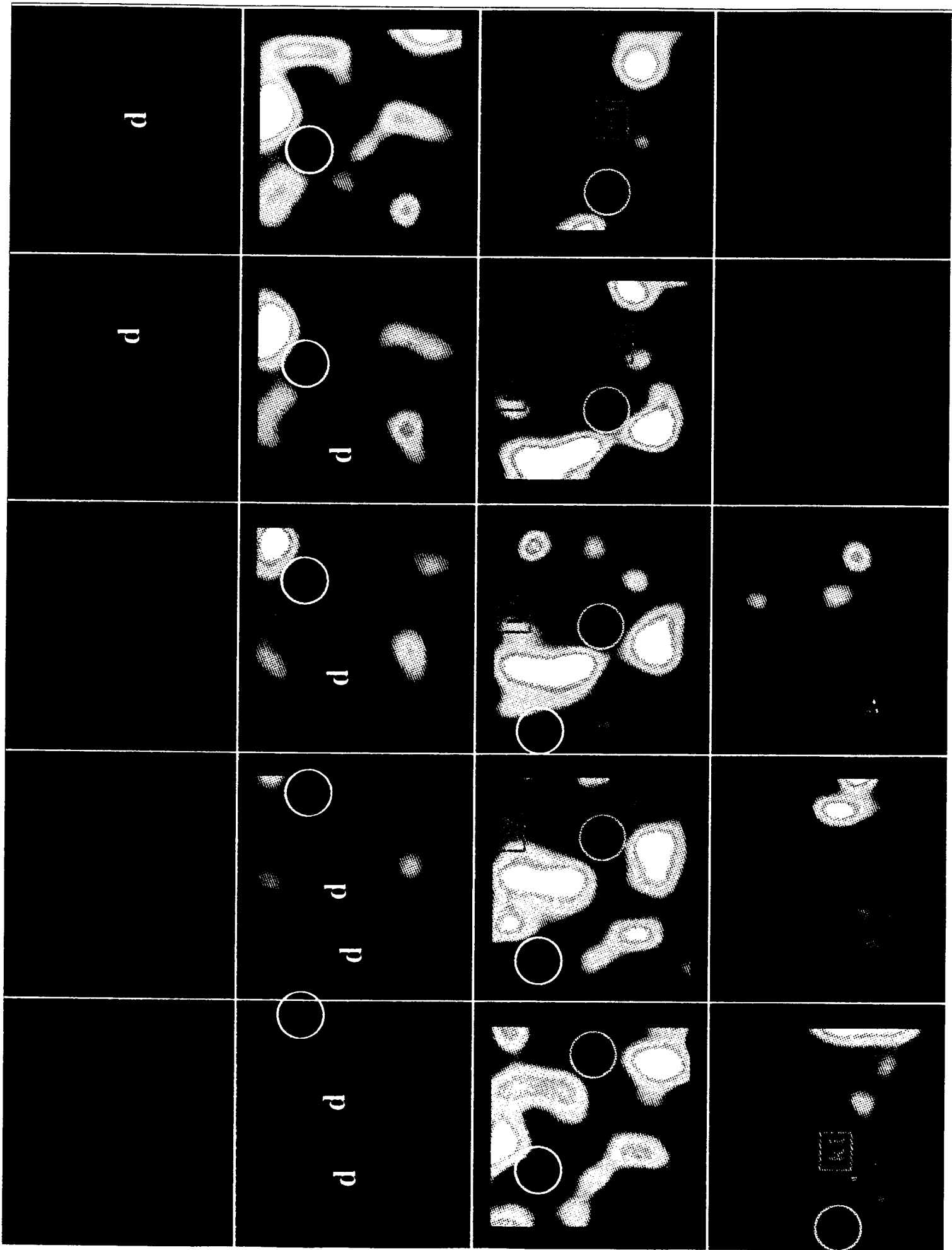
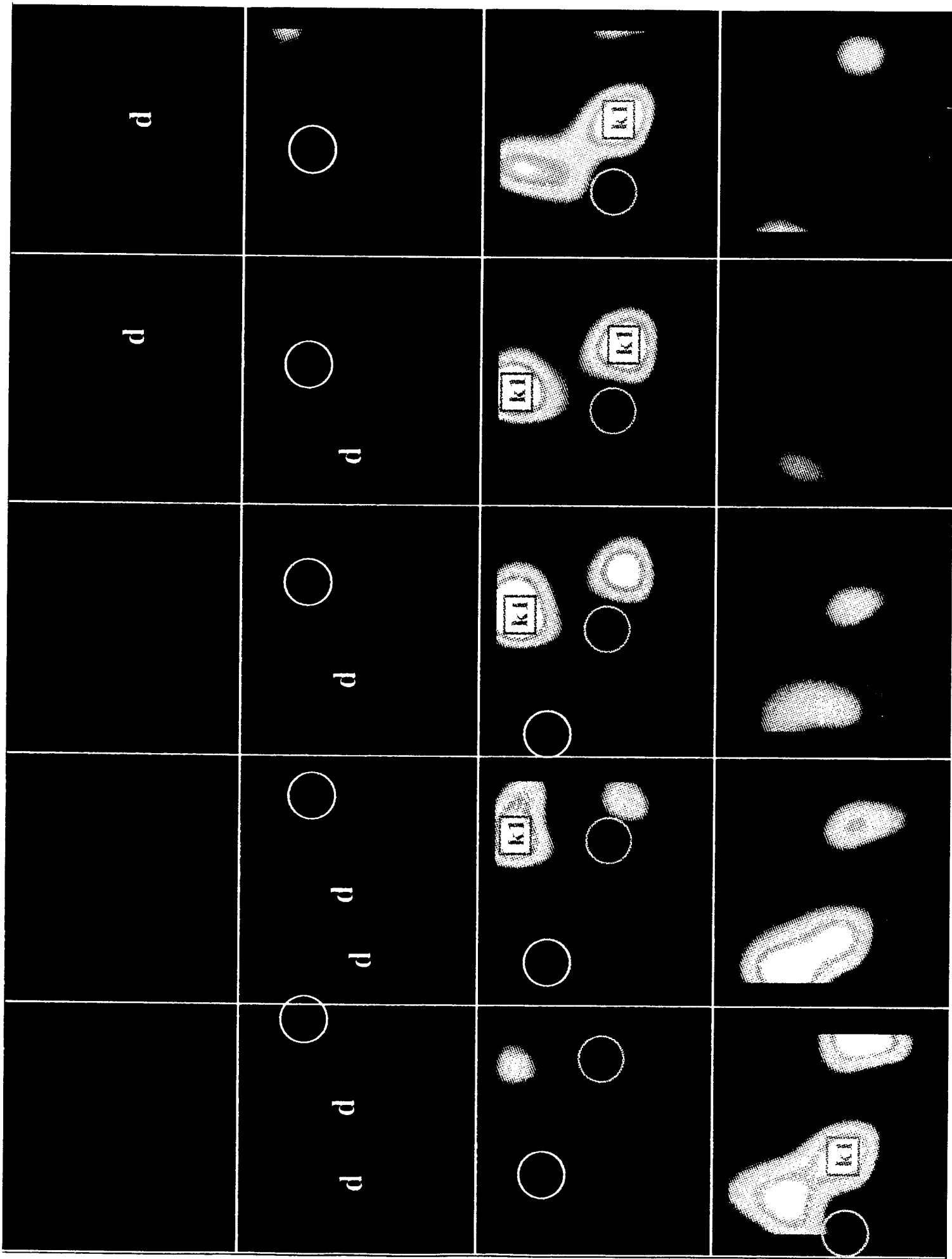
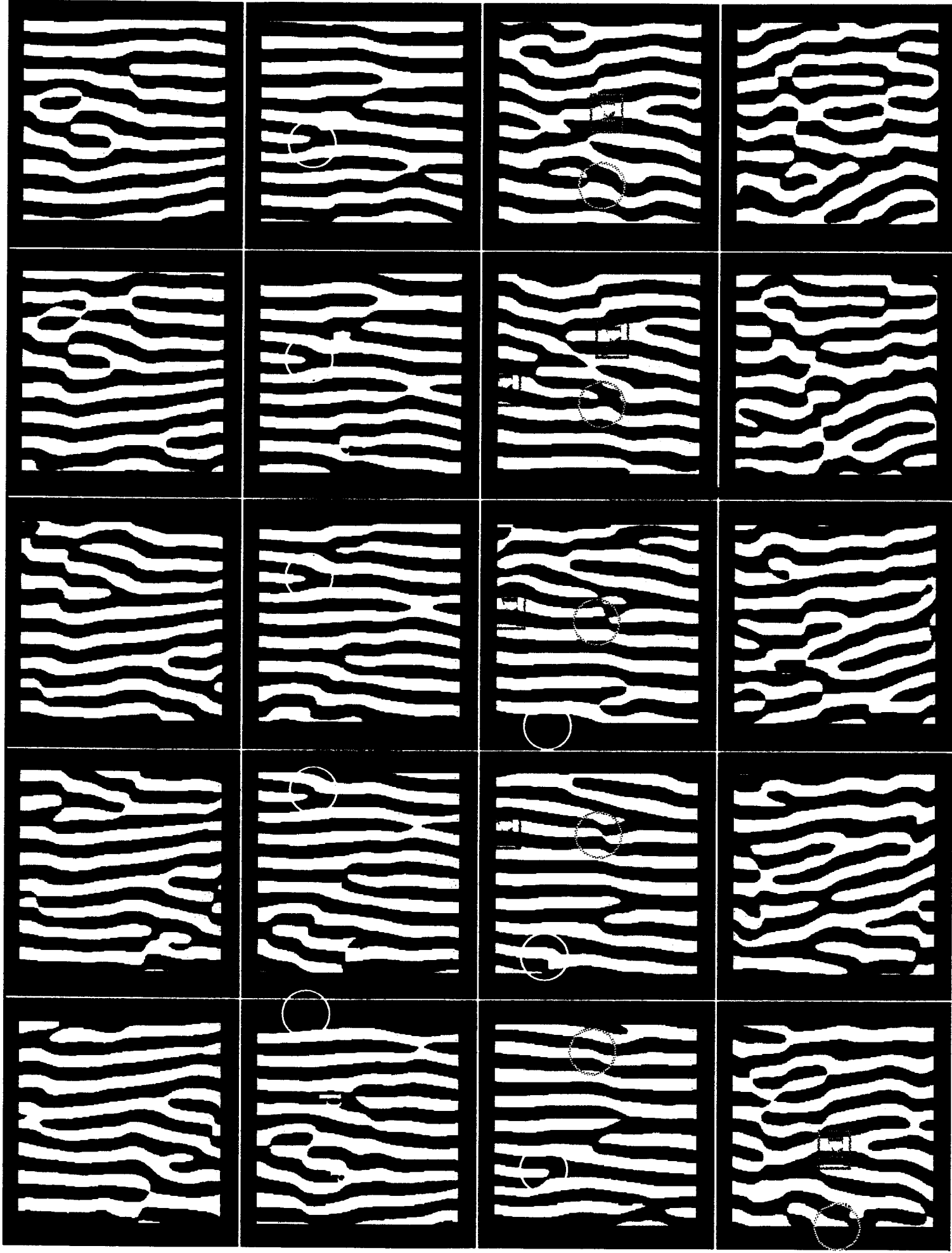


Fig 5

Fig 6





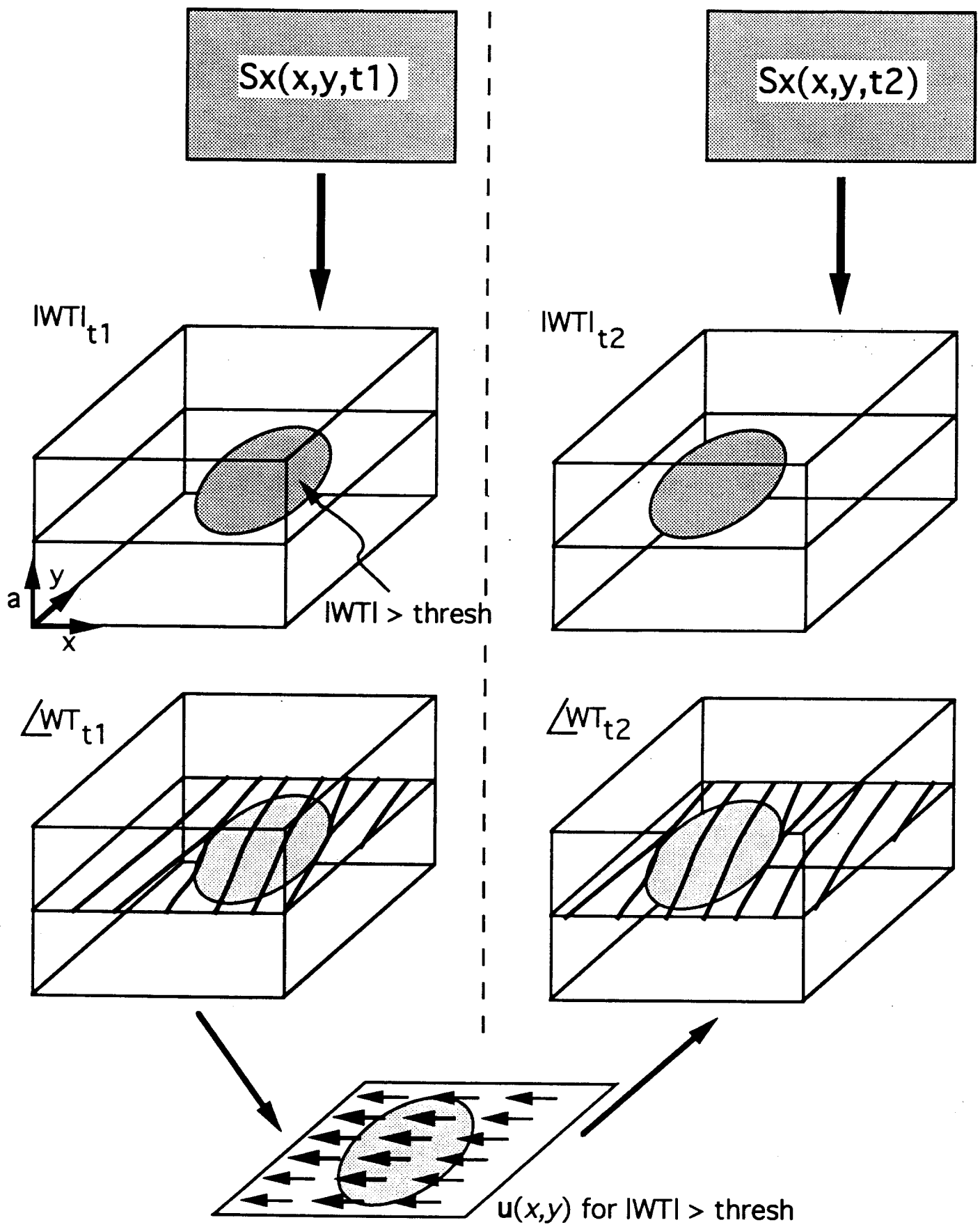


Fig. 8

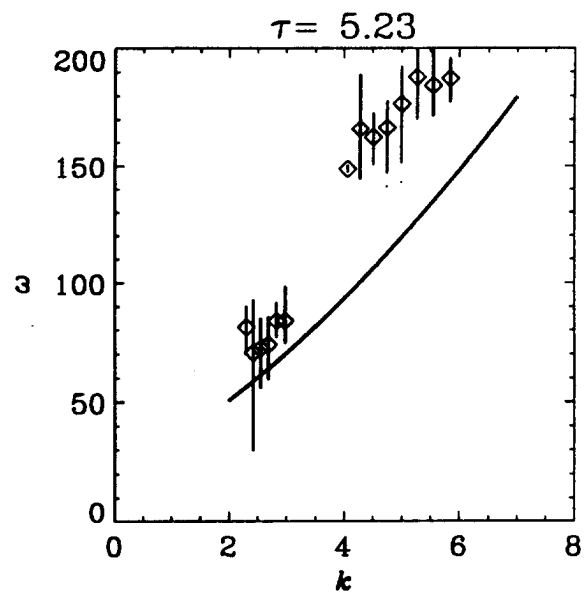
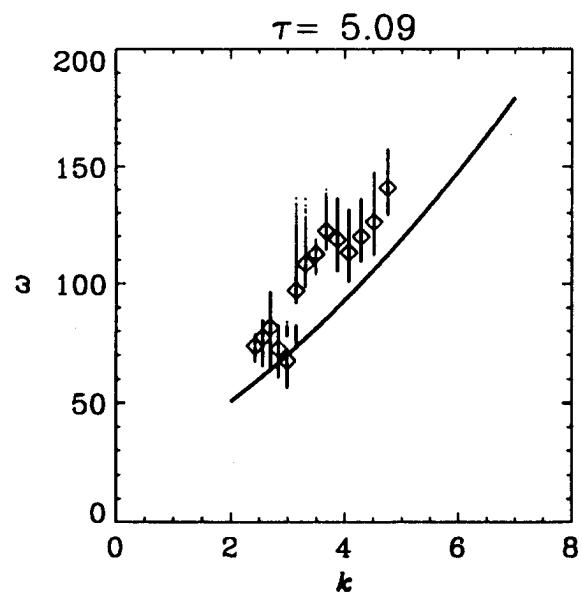
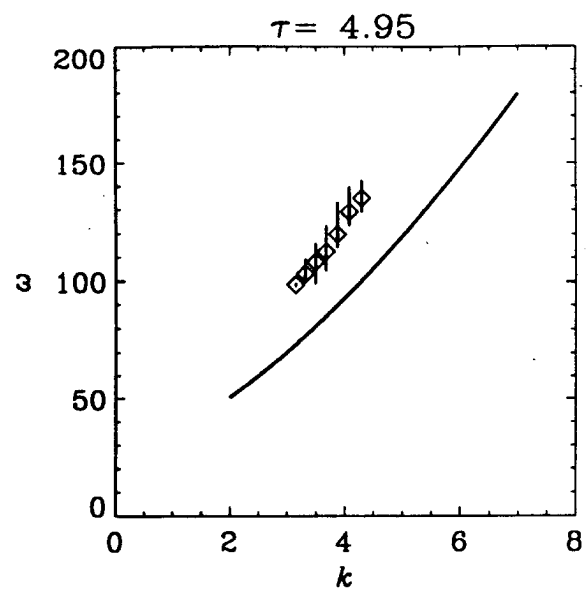
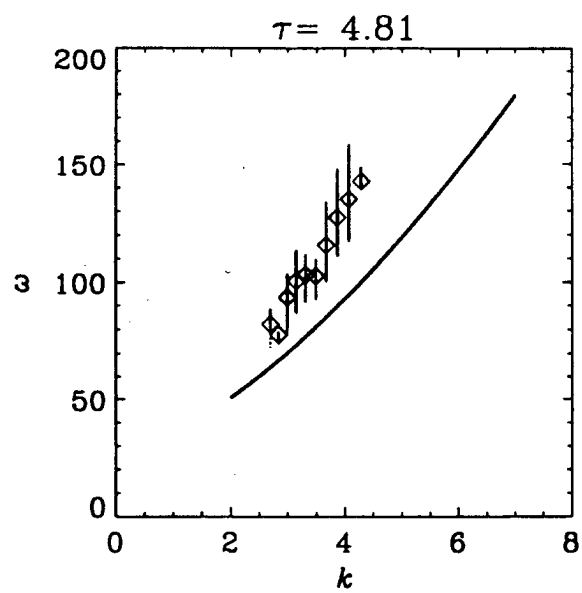


Fig. 9

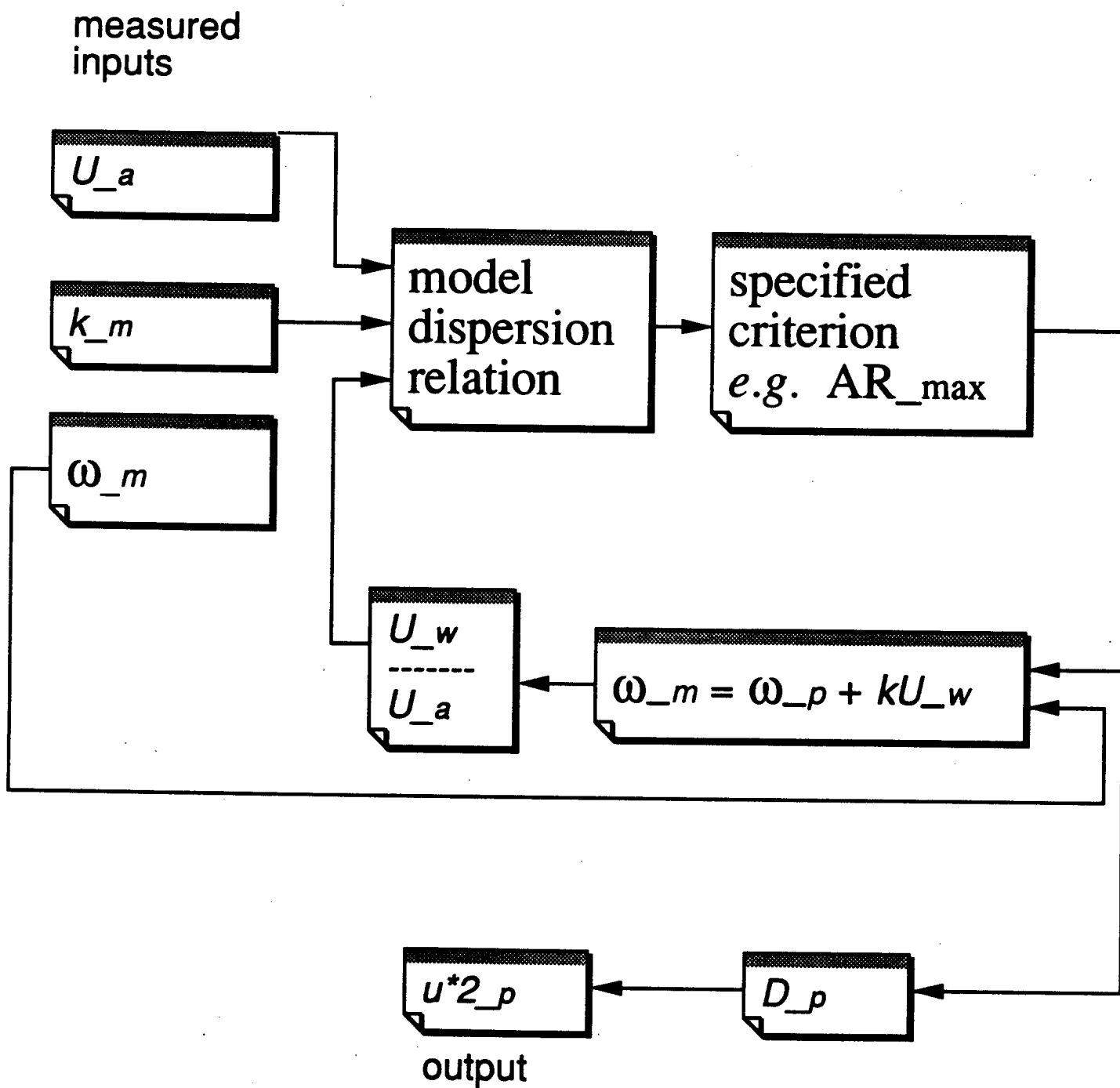


Fig. 10

Estimating $\bar{\omega}(\vec{k})$ in an Unsteady, Wind-Generated Surface Wave Field from the 2D Complex Wavelet Transform of the Surface Slope

G.R. Spedding
*Department of Aerospace Engineering,
University of Southern California, Los Angeles.*

J. Klinke
*Scripps Institute of Oceanography,
University of California, San Diego.*

and

S.R. Long
*NASA GSFC/WFF,
Wallops Island, Virginia.*

October 31, 1994

Abstract. The initial formation and growth of capillary-gravity waves under wind-induced surface stress is studied by measurement of the instantaneous, 2D distribution of the alongwind slope at a fixed fetch. A new technique, using information from the complex 2D wavelet transform, is described for the calculation of the local, instantaneous dispersion relation. The technique is validated on simple test fields. The dispersion relation measured from the wave tank data is consistent with predictions from linear stability theory at early times, but departures can be noted later on. Some physical interpretations are offered, and possible nonlinear mechanisms are discussed.

Key words: wavelet transform, dispersion relation, nonlinear waves

1 Introduction

Classical linear stability analysis has been partially successful in predicting the generation and growth of the initial wave field on a calm water surface following an impulsive start in the wind stress. However, neither the Phillips resonant interaction [1, 2], nor the Miles critical layer instability mechanism [3, 4] has been able to incontrovertibly account for laboratory and field measurements of growth rates and wave initialisation. Kawai [5] made careful measurements of the initial growth of wind generated surface waves, and combined this with a stability analysis by numerical integration of the Orr-Sommerfeld equation with initial and boundary values suggested by the experimental data. It was found that linear, shear flow instability mechanisms could successfully predict growth rates, phase speeds, and wavenumber-frequency relations in the observed wave field, to within experimental accuracy. It was further pointed out that the subsequent evolution of long-crested to short-crested waves could not be expected to be governed by linear mechanisms, as indeed was indicated by 'complicated movements of spectral peaks'. These spectra were quasi-steady estimates, computed by the maximum entropy method

(cf [6]) on data segmented in time.

Following recent advances in local space-scale decompositions by means of wavelet functions, it is now possible to perform a systematic quantitative analysis of such unsteady phenomena, without some of the limitations imposed by the Fourier decomposition, and where the balance between resolution in physical and spectral space, scales automatically with wavenumber, within the limits prescribed by the uncertainty principle. The objective of this paper is to describe the development of a method for the measurement of spatially-localised frequency and wavenumber relations of unsteady wind-generated surface waves, and to give examples of its initial application to recent, *2D*, instantaneous wave slope data. This will include the later times when nonlinear mechanisms may be anticipated to be significant.

2 Experimental data

The experiments were conducted at the NASA Wallops wind-wave interaction facility, which is described in detail in [7]. The aspects of significance to this paper are shown in Fig. 1. Air is drawn by suction over a 75 cm deep water channel over a working section of approximately 18m length and 0.9m width. The air gap over the still water surface is 46 cm. Observations of the streamwise surface slope were made at a fetch of 6.5m, using an Imaging Slope Gauge (ISG) with a field of view of approximately 18.5 x 14cm. The single experimental run treated here was made with a mean reference velocity, $U_5 = 5.2 \text{ m.s}^{-1}$ (measured 5cm above the surface, and 15 cm upstream of the ISG). Digitising of the video-encoded CCD signal began 7s after the fan was turned on, at which time $U_5 = 5.0 \text{ m.s}^{-1}$. By frame#50, 8.6s after fan-on, the steady value of U_5 had been reached. The x , y and z axes of a Cartesian coordinate system run streamwise, spanwise, and vertically up from the water surface, respectively.

The physical problem is thus somewhat complicated – not only does it involve temporal and spatial growth of viscous boundary layers in both water and air, but the initial conditions and start up are much less homogeneous in space and instantaneous in time, than one would perhaps prefer, and careful physical interpretations must be made in this light.

The ISG works on principles described in [8]. A strong, homogeneous (in y) light source illuminates a rectangular box filled with particles in suspension that scatter the light so that its intensity decreases with downstream distance. In the absence of any surface deformation, light rays pass normal through the surface and the CCD illumination is also homogeneous in y , monotonically decreasing in x . A nonzero surface slope in x (s_x) causes light rays to be refracted and arrive at a different x location on the sensor array. Thus, given the intensity distribution on the array, it is possible to compute the deflection and, hence, the value of s_x at each position in $\{x, y\}$. With careful calibration procedures [9], this calculation can be performed so as to reduce errors due to nonlinear effects to less than $0.05|s_x|$.

Fig. 2 shows a time sequence of s_x over a 1.5 second period, during which time the mean and maximum slopes increase by more than a factor of 10. Even at early times, the wave field is never strictly one-dimensional, or uniform in y . It is unclear as to how much this reflects the inhomogeneity of the original forcing. At frame#70, $s_x(x, y)$ reaches its most ordered state, in which the spanwise correlation length is a maximum. After this, the spanwise correlation length decreases, and shortly after the end of this sequence the wave field becomes quite disordered, as noted originally by Kawai [5], and more recently in [10].

3 2D Wavelet functions for 2D data

A very readable introduction [11] and review of wavelet applications [12] have recently become available, and the specific design and application of 2D wavelet functions for analysis of 2D real signals is discussed in [13]. Denoting $f_W(a, \vec{b})$, as the wavelet transform (WT) of the function $f(\vec{x})$, a is the analysing wavelet scale, and resonance at any particular value of a can be related to a wavenumber \vec{k} in the signal. This information is *localised* at a shift from the origin, \vec{b} , equivalent to physical location \vec{x} .

It is convenient to think of the wavelet transform as a product in Fourier space of the wavelet function $\hat{g}(a\vec{k})$ with the Fourier-transformed signal, $\hat{f}(\vec{k})$, and [13] introduced the *Arc* wavelet as a smooth function for general use in a complex, non-directional specific, energy-conserving WT for 2D data analysis. Here, the alongwind surface slope is $s_x = \partial s / \partial x$, and since $s_x(x, y)$ also contains contributions from $s_y(x, y)$ projected on x , the response ought to be weighted by $\cos \theta$, where θ is the angle between \vec{k} and the mean wind, U_∞ . We therefore introduce the *Cos* wavelet function:

$$\begin{aligned} \vec{k} \in \pi^1 & : \hat{g}(a\vec{k}) = \hat{g}(a\vec{k}) = \cos \theta \exp \left(-\frac{a^2 \sigma^2 (|\vec{k}| - |\vec{k}_0|/a)^2}{2} \right) \\ \vec{k} \in \pi^2 & : \hat{g}(a\vec{k}) = 0, \end{aligned} \quad (1)$$

where $\theta = \overline{(k_x, \vec{k})}$. It describes a cosine-weighted arc in wavenumber space with Gaussian cross-section, centred at, and shifted from the origin by $|\vec{k}_0|/a$, with width $1/(\sigma a)$. Isometric surfaces of the *Cos* function in wavenumber and physical space are shown in Fig. 3. Owing to the smooth decay in \hat{g}_{Cos} , g_{Cos} has improved localisation in physical space over the original g_{Arc} .

The *Cos* WT can be computed at each timestep from $s_x(x, y)$, and the result can be expressed as the amplitude $|f_W(a, \vec{b})|$, and the phase, $\angle f_W(a, \vec{b})$ of the complex WT.

4 How to calculate $\vec{\omega}(\vec{k})$ from $f_W(a, \vec{b}, t)$

Since one has local phase information from the complex WT, then the vector field \vec{u} that performs the mapping of,

$$\mathcal{L}f_W(a, \vec{b})_{t_1} \xrightarrow{\vec{u}} \mathcal{L}f_W(a, \vec{b})_{t_2}, \quad (2)$$

where $\mathcal{L}f_W(a, \vec{b})$ is known at two closely-spaced timesteps, t_1, t_2 , can be used to estimate a local frequency. Since \vec{u} is measured at fixed wavelet scale, a , it is associated with wavenumber $|\vec{k}|$, and

$$\vec{\omega} = |\vec{k}|\vec{u}. \quad (3)$$

Various methods can be devised for computing \vec{u} . Although details will not be given here, a hybrid scheme using a novel combination of optical flow and cross-correlation methods was found to work reliably. [14] can be consulted for overviews of each of these classes of methods separately. The 2D spatial cross-correlation seeks to find the local displacement, \vec{r} , at discrete interrogation windows, such that

$$C(\vec{r}) = \sum_{\vec{x} \in R} f(\vec{x}, t_1) f(\vec{x} + \vec{r}, t_2) \quad (4)$$

is maximised, and then

$$\vec{u} = \vec{r}/(t_2 - t_1).$$

However, simple solutions to this problem blow up in the presence of the *local* phase discontinuities of $\pm\pi$ found in $\mathcal{L}f_W(a, \vec{b})$, and it is desirable to find some globally smooth solution, such as commonly computed using optical flow techniques.

\vec{u} was computed using a modification of the technique of [15] who kindly made available their original codes. We proceed by minimising the cost function,

$$e(\vec{u}) = \int_{\Omega} \{e_I(\vec{u}) + \gamma_1 e_s(\vec{u}) + \gamma_2 (\nabla \cdot \vec{u})^2\} d\Omega. \quad (5)$$

$e_I(\vec{u})$ and $e_s(\vec{u})$ are terms related to the L_2 error, and the smoothness (both global terms), respectively, and γ_1 and γ_2 are weightings on the smoothness, and a divergence-free constraint that was introduced by [15] for fluid flow applications.

When the displacement field due to \vec{u} is large compared to the grid resolution, a multiresolution relaxation method is used to avoid convergence on local minima in eq.(5). Beginning from the original data, successive binary expansions are performed until the local displacements do not exceed one mesh size. Given an initial estimate of the flow field, the solution at any level n is interpolated out to level $n+1$ and used as the initial approximation for the $n+1^{th}$ iteration. Circular Gaussian functions were used for the pyramid expansion, and a conjugate-gradient method was used for the iterative solution of successive linear approximations to eq.(5).

The choice of weights $\gamma_{1,2}$, was made empirically following extensive numerical experiments on synthetic wave fields. These test also showed that the multiresolution optical flow (MROF) method could *not* be relied upon to give the correct absolute value for a constant, smooth displacement field, over a large range of displacements, for fixed $\gamma_{1,2}$. This is problematic, since the variation of \vec{u} with $|\vec{k}|$ is of particular interest. A convenient and reliable solution turns out to be to use a cross-correlation method in order to generate the initial first estimate for the lowest resolution optical flow computation. Owing to the grid expansion, the *local* behaviour of eq.(4) is not a liability, and one immediately benefits from a very accurate first estimate. The optical flow computation then preserves an expansion of this initial estimate while maintaining a γ_1 -weighted global smoothness. Further numerical experiments confirmed the robustness of this hybrid technique (XMROF) over a range of displacement magnitudes.

A block diagram summarising the calculation methods, from initial digitised data to $\vec{\omega}(\vec{k})$ is given in Fig. 4. The local frequency, ω is computed from eq.(3) for all $|f_W(a, \vec{b})| > |f_W(a, \vec{b})|_{thresh}$. The threshold value was set to 80% of the maximum value of $|f_W(a, \vec{b})|$ at each timestep.

Extensive numerical simulations were performed on synthetic data fields, and on $\angle f_W(a, \vec{b})$ derived from real data, but given a known form of $\vec{\omega}(\vec{k})$. These results will be reported in detail elsewhere. In general, the mean difference between spatially-averaged estimates of $\vec{\omega}(\vec{k})$, and the true value, was always less than 5% in ω and less than 10% in $|\vec{k}|$. In conditions closely matching the experimental signal to noise ratios and resolution in \vec{x} and t , the mean errors were about half that.

5 Time dependent, local, dispersion relation for wind-generated surface waves

Although measurements are available for $\vec{\omega}(|\vec{k}|, x, y)$, they will be averaged over $\{x, y\}$ and plotted only for $|\vec{\omega}|$ for brevity and ease of comparison. This dispersion relation is plotted for 3 timesteps in Fig. 5(a-c). Fifteen frames separate each plot, which therefore represents data from a completely new wavefield that has convected into the measuring location. The measured data points can be compared with the dispersion relation that can be derived from the linearised momentum and continuity equations at the interface, as given by Caponi *et al.*[16],

$$\omega = \sqrt{(gk(1 - \alpha) + \sigma k^3)}, \quad (6)$$

where α is the ratio of air to water density ($= 1.21 \times 10^{-3}$), g is the acceleration due to gravity, and σ is the surface tension ($74 \text{ cm}^3\text{s}^{-2}$). The measured phase speeds are doppler-shifted by the water drift velocity at the surface, U_0 . Since we lack accurate simultaneous measurements of U_0 , a constant offset is added to place the solid curve on the data point occurring at the predicted most amplified

wave, at $k_0 = 3.63 \text{ rad.cm}^{-1}$ (An independent measurement of the wavenumber of the most amplified wave from the spatially-averaged centroid of the $|WT|^2$ gives $k_0 = 3.67 \pm 0.05 \text{ rad.cm}^{-1}$). This offset gives a drift current of 14 cm.s^{-1} , which is consistent with previous results reported for this facility [17], but at $.027U_\infty$ is significantly below the .05 or $.04U_\infty$ sometimes assumed in the literature.

The measured $\omega(|\vec{k}|)$ in Fig. 5a agrees with the theoretical prediction to within experimental uncertainty over the whole range of $|\vec{k}|$ where there is significant energy. At the next timestep (Fig. 5b), the range of energetic $|\vec{k}|$ has contracted around k_0 , consistent with qualitative observations made earlier for Fig. 2 at $t=65/70$. The agreement with the linear theory over this range remains good. At $t=80$, the range of energetic modes is significantly expanded, with energy having appeared in both lower and higher wavenumbers. It is greatly reduced around k_0 . Above k_0 , eq.(6) predicts the data well, but there is increased scatter and difference between the two at, and below k_0 .

6 Discussion & Conclusions

The simple relationship of eq.(6) from 1-D linear theory appears to hold well until the latter stages of the sequence discussed here, despite the fact that the wavefield is never strictly 1-D (i.e. spanwise uniform). Nevertheless the initial, most unstable wavelength is well predicted. Caponi *et al.* [16] include a discussion of the time-varying interpretation of their analytical results, which were obtained from piecewise linear approximations to the wind and water velocity profiles, although the solution itself did not involve time-dependent growth of these profiles. Quite specific predictions are made concerning the growth rates and most unstable modes at different wind speeds and we look forward to making detailed comparisons over the same parameter range. The results of Kawai [5] thus far appear to be confirmed in the current study, and will also be compared further.

At the later stages corresponding to the presumed onset of nonlinear effects, we note here growth of modes of both higher and lower wavenumber than k_0 . This is illustrated in Fig. 6, where it appears that growth of these modes occurs in closely associated spatial locations. Although an earlier, preliminary wavelet analysis [10] indicated that significant energy developed in subharmonic wavelengths, the improved resolution and quantitative accuracy of the current data allow the distinction to be made that the majority of the sideband growth actually occurs in bands centred at $\frac{2}{3}k_0$ and $\frac{4}{3}k_0$. The sum of these is $2k_0$, consistent with the resonance frequency condition for a Benjamin-Feir type instability. However, Bliven *et al.* [18] suggested that this mechanism is suppressed by active wind forcing, and it is unlikely to be significant at this scale range. There is an alternative, simple physical interpretation, that asymmetric steepening and growth of single wave crests is manifested as different modes which would then necessarily be correlated in physical space.

In this case, the natural tendency to think in terms of Fourier modes, or their

spatially localised, wavelet-based cousins, may be unnecessarily restrictive. It could prove interesting instead to allow the wavelet function basis itself to auto-adapt with time, similar in spirit to the work of Coifman and colleagues [19, 20].

Acknowledgements

This work was performed under Grant no. N00014-92-J-1615 in the Nonlinear Ocean Waves program sponsored by the US Office of Naval Research. Their support, and encouragement from the initial program director, Alan Brandt, is greatly appreciated. Additional support from the Oceanic Processes Program of NASA is also gratefully acknowledged. The essential inputs from Prof. FK Browand, Dr B Jähne and Dr NE Huang are acknowledged with pleasure and GRS thanks Kelly for invaluable assistance with the figures.

References

1. OM Phillips. On the generation of waves by turbulent wind. *J. Fluid Mech.*, 2:417–445, 1957.
2. OM Phillips. *The Dynamics of the Upper Ocean*. Cambridge University Press, 1977.
3. JW Miles. On the generation of surface waves by shear flows. *J. Fluid Mech.*, 3:185–204, 1957.
4. JW Miles. On the generation of surface waves by shear flows. part 2. *J. Fluid Mech.*, 6:568–582, 1959.
5. S Kawai. Generation of initial wavelets by instability of a coupled shear flow and their evolution to wind waves. *J. Fluid Mech.*, 93:661–703, 1979.
6. WH Press, SA Teukolsky, WT Vetterling, and BP Flannery. *Numerical Recipes in FORTRAN: The Art of Scientific Computing*, pages 565–569. Cambridge University Press, Cambridge, second edition, 1992.
7. SR Long. NASA Wallops Flight Facility: Air-Sea Interaction Research Facility. Technical Report 1277, NASA GSFC/WFF, Wallops Island, VA, 1992.
8. B Jähne and K Riemer. Two-dimensional wave number spectra of small-scale water surface waves. *J. Geophys. Res.*, 95:11531–11546, 1990.
9. B Jähne and H Schultz. Calibration and accuracy of optical slope measurements for short wind waves. In *Optics of the Air-Sea Interface: Theory and Measurements*. SPIE, 1992.
10. GR Spedding, FK Browand, NE Huang, and SR Long. A 2-D complex wavelet analysis of an unsteady wind-generated surface wave field. *Dyn. Atmos. Ocean*, 20:55–77, 1993.
11. Y Meyer. *Wavelets: Algorithms and Applications*. SIAM, Philadelphia, 1993.
12. MB Ruskai, G Beylkin, R Coifman, I Daubechies, S Mallat, Y Meyer, and L Raphael, editors. *Wavelets and their Applications*. Jones and Bartlett, Boston, 1992.
13. T Dallard and GR Spedding. 2-D wavelet transforms: Generalisation of the Hardy space and application to experimental studies. *Eur. J. Mech. B/Fluids*, 12:107–134, 1993.
14. B Jähne. *Digital Image Processing. Concepts, Algorithms and Scientific Applications*, pages 275–317. Springer-Verlag, Berlin, 1991.
15. Z Zhou, CE Synolakis, RM Leahy, and SM Song. Calculation of 3-D internal displacement fields from 3-D x-ray computer tomographic images. *J. Appl. Mech.*, 1993. submitted.
16. EA Caponi, MZ Caponi, PG Saffman, and HC Yuen. A simple model for the effect of water shear on the generation of waves by wind. *Proc. R. Soc. Lond. A*, 438:95–101, 1992.
17. NE Huang. Laboratory investigations of ocean surface roughness generation. In A Brandt, SE Ramberg, and MF Shlesinger, editors, *Nonlinear Dynamics of Ocean Waves*, pages 128–149. World Scientific Press, Singapore, 1992.

18. LF Bliven, NE Huang, and SR Long. Experimental study of the influence of wind on Benjamin-Feir sideband instability. *J. Fluid Mech.*, 162:237–260, 1986.
19. RR Coifman, Y Meyer, and V Wickerhauser. Wavelet analysis and signal processing. In MB Ruskai, G Beylkin, R Coifman, I Daubechies, S Mallat, Y Meyer, and L Raphael, editors, *Wavelets and their Applications*, pages 153–178. Jones and Bartlett, Boston, 1992. see also publications and software available at pascal.math.yale.edu.
20. MV Wickerhauser. Acoustic signal compression with wavelet packets. In CK Chui, editor, *Wavelets - A Tutorial in Theory and Applications*, pages 679–700. Academic Press, San Diego, 1992.

7 Figure Captions

Figure 1. Simplified schematic of the wind-wave generation facility. The x's mark approximate locations of pitot tubes, and a capacitance wire probe for wave elevation is marked by an 'o'. The fan control, 1D digitising of pitot tube and wave height data, and sampling of the 2D video signal are synchronised using 3 personal computers and one Sun workstation.

Figure 2. Time sequence of surface slope values computed from the ISG measurements, numbered in frames. Since the sampling rate, determined by the video framing rate, is 30Hz, the total sequence, occupying 45 frames, covers 1.5 seconds. The doppler-shifted group velocity is such that an entirely new wave field is covered every 15 frames. The color bar is scaled to cover the maximum and minimum slope symmetrically about zero at the last time step in the sequence.

Figure 3. The *Cos* wavelet function in Fourier space (a), and its real and imaginary parts (b) & (c) in physical space.

Figure 4. Block diagram summary of the method for calculating $\vec{\omega}(|\vec{k}|)$ from $s_x(x, y)$. Currently, the minimum Δt is determined by the video framing rate. The two video fields are treated identically on either side of the line of symmetry in the block diagram, until the XMROF method combines both sides to calculate $\angle WT_{t_1} \mapsto \angle WT_{t_2}$. All boxes marked with an asterisk include state-of-the-art advances in analytical techniques from the last 2 years.

Figure 5. Evolution of the dispersion relation for the wind-generated surface wave field of Fig. 2. (a) $t=50$, (b) $t=65$, (c) $t=80$. Diamonds are the mean measured values at each $|\vec{k}|$. The solid line is from eq.(6), drawn over the whole range of k for which the WT was computed.

Figure 6. Isosurface of $|f_W(a, \vec{b})|$, thresholded at 50% of the maximum, for $t=80$. Surface intensity variations are only to assist in showing the 3D shape. The vertical scale, a runs from $\lambda_{max} = 4.6\text{cm}$ at the bottom, to $\lambda_{min} = 0.6\text{cm}$ at the top.

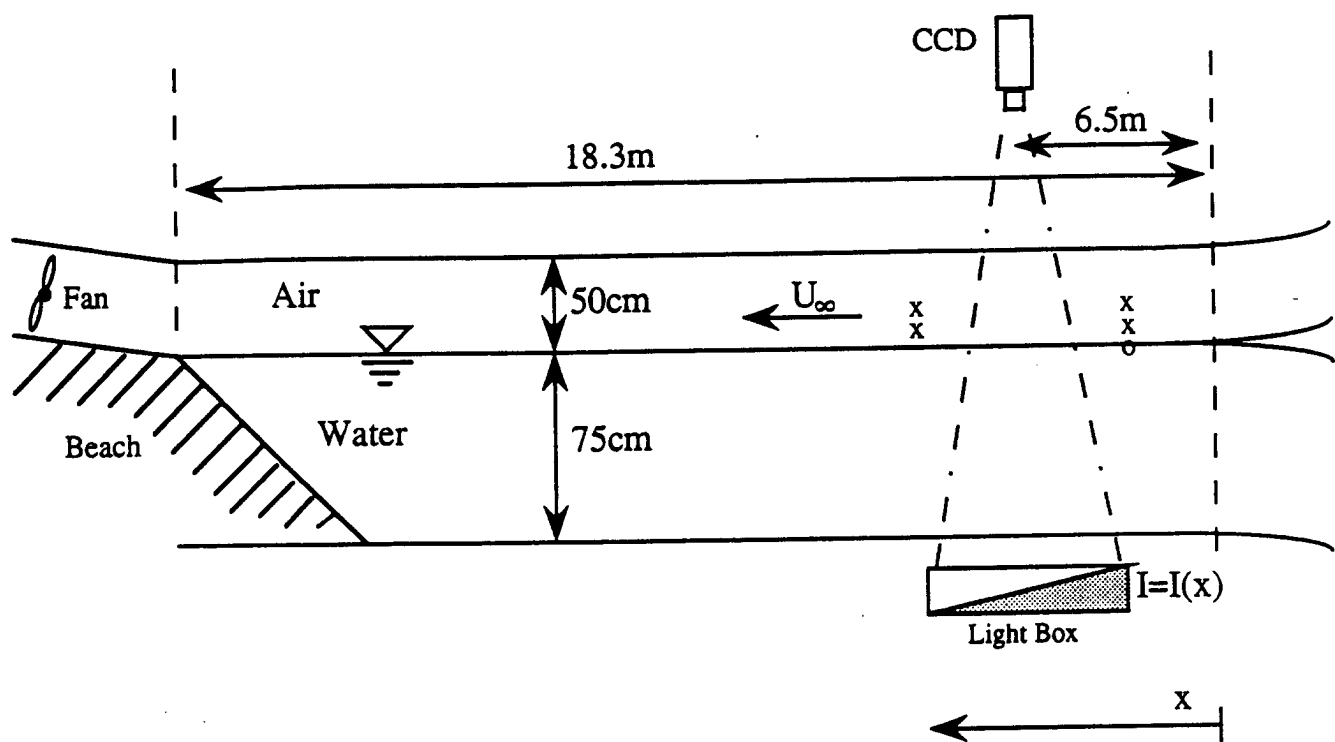


Fig. 1

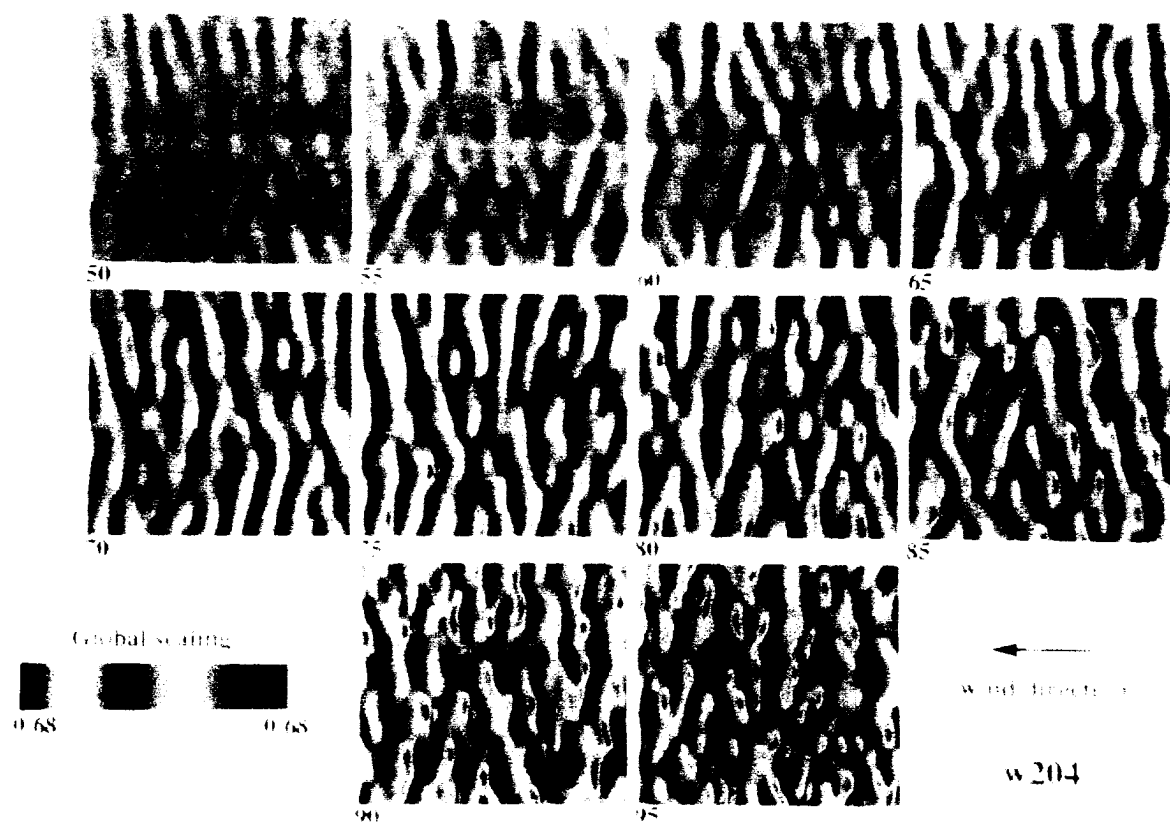


Fig. 2

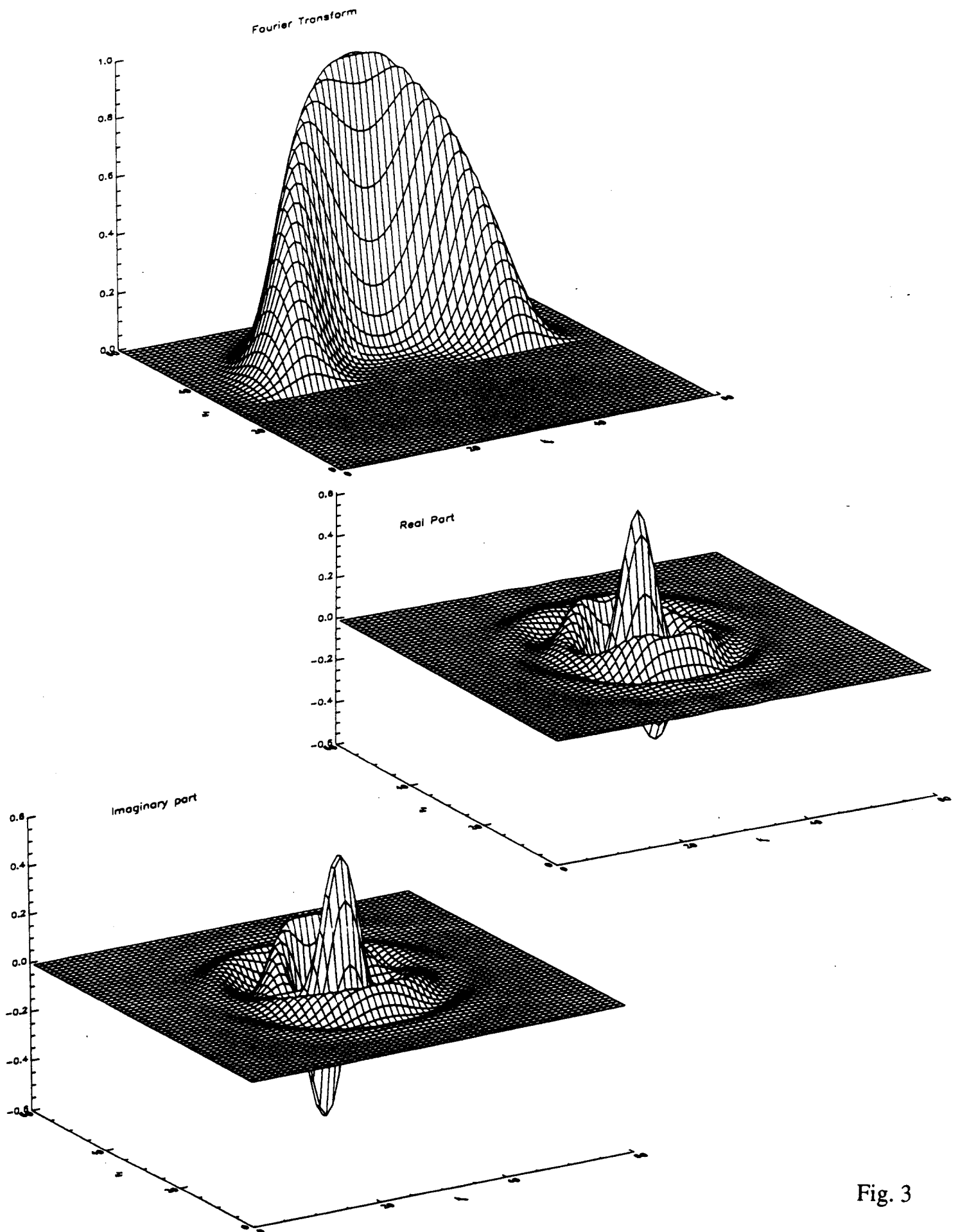


Fig. 3

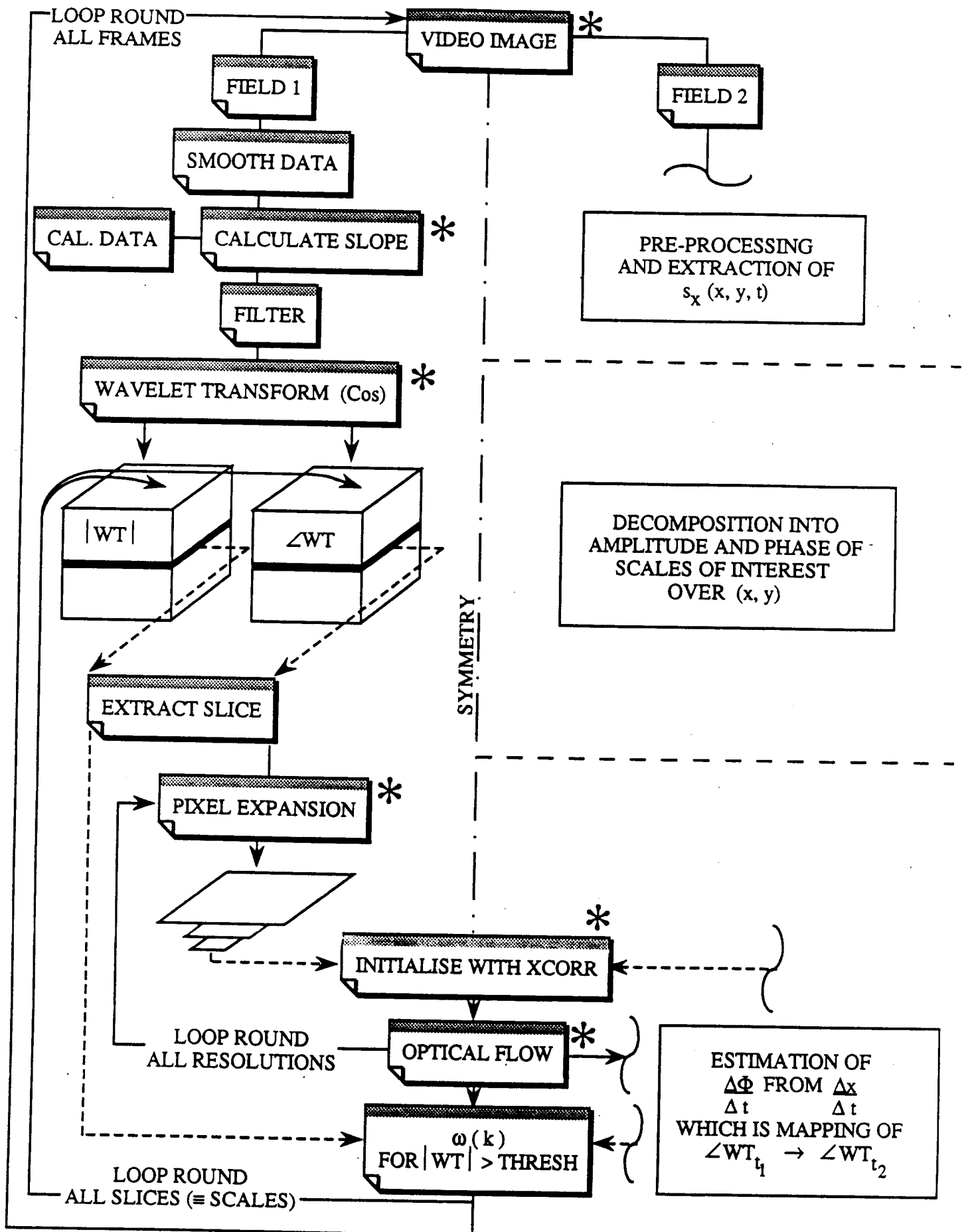


Fig. 4

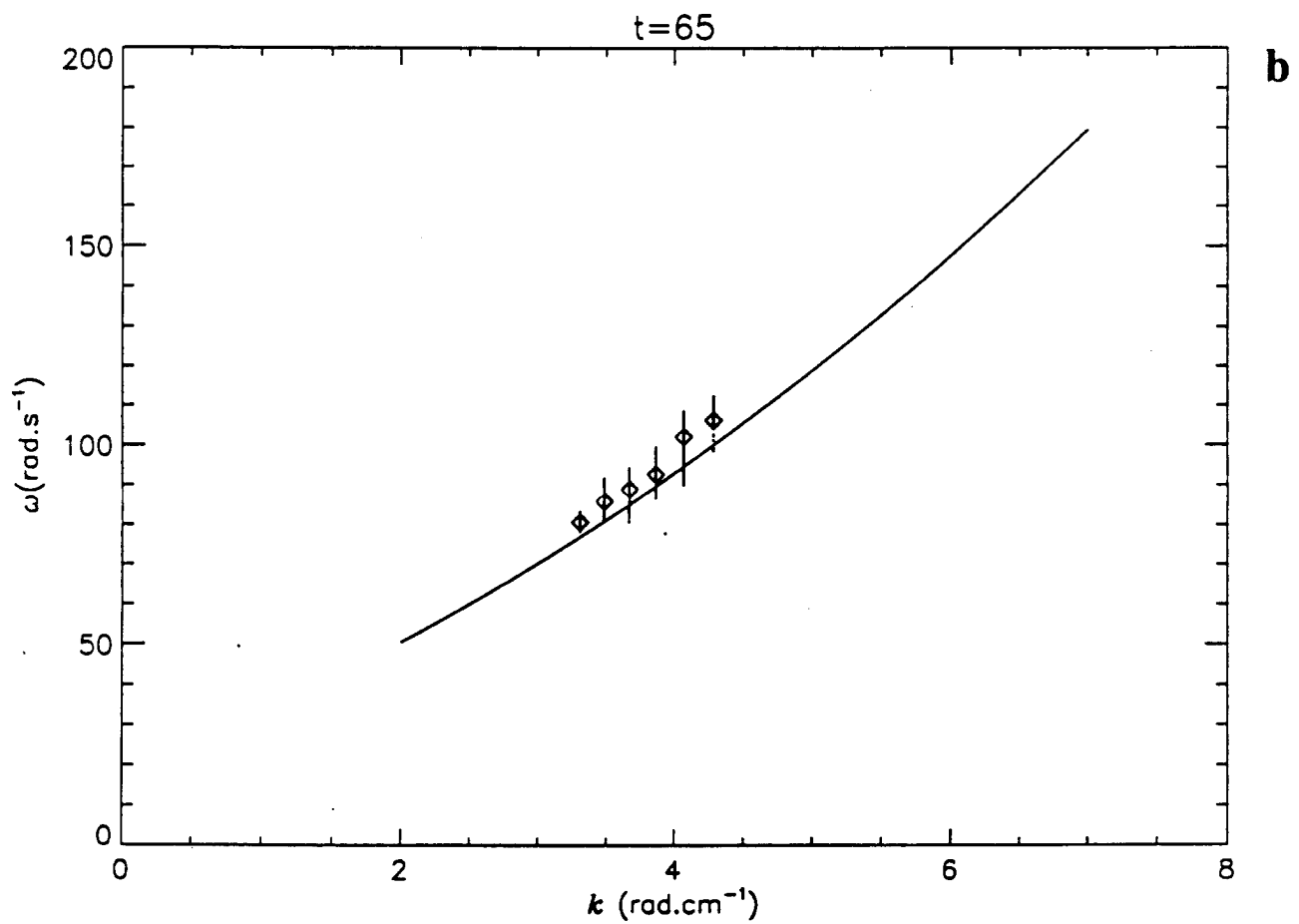
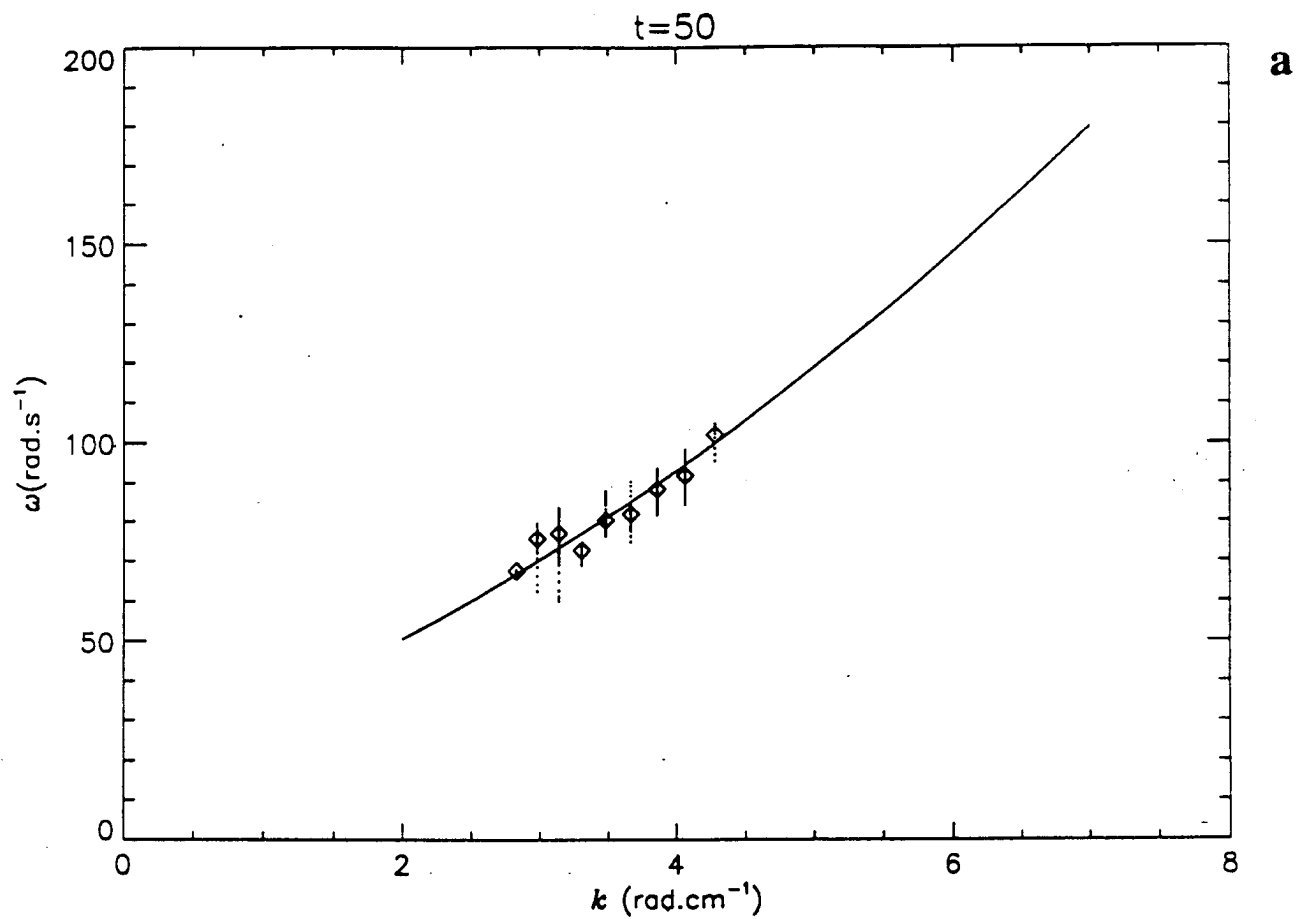


Fig. 5

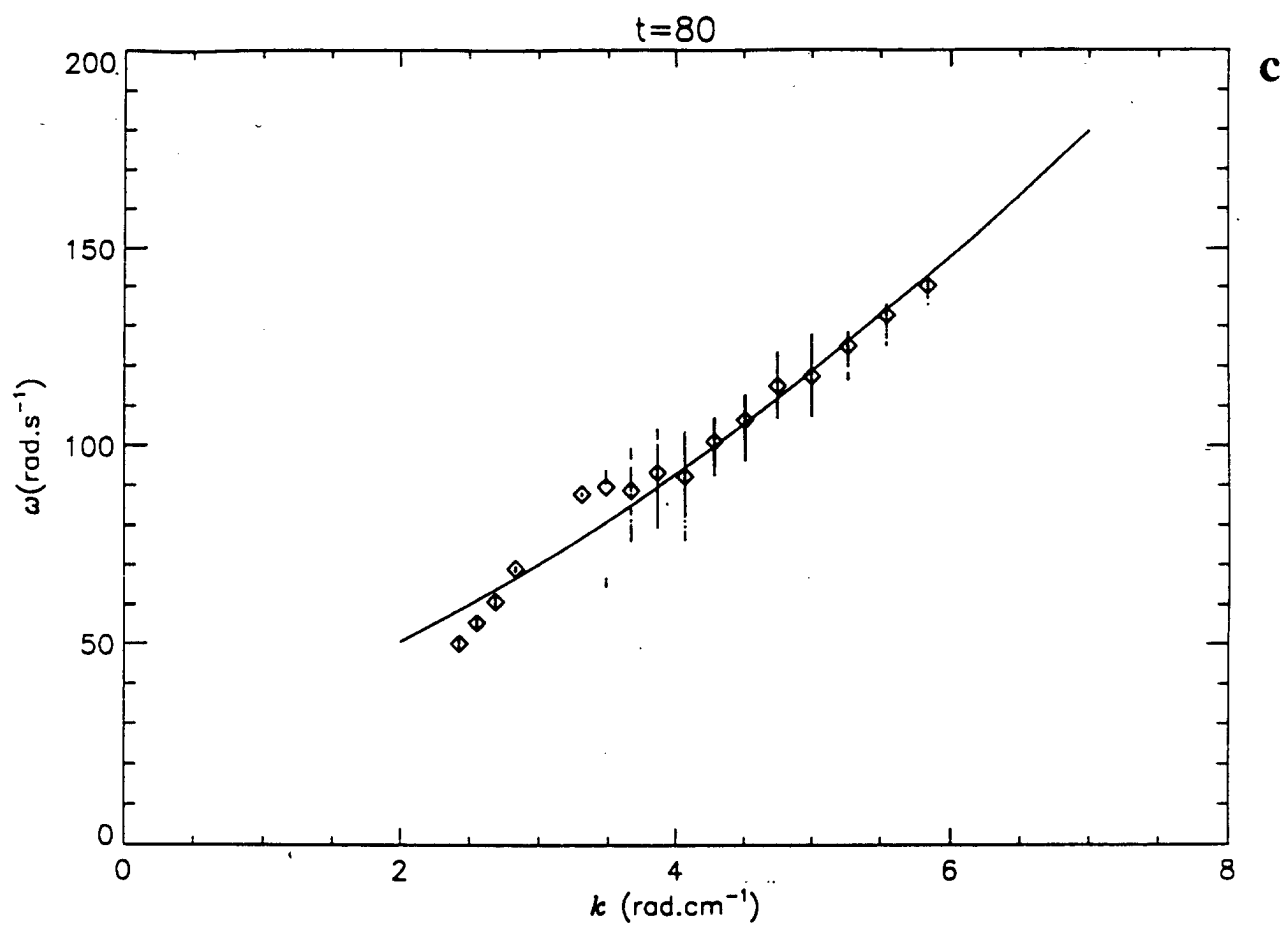


Fig. 5 [cont]



Fig. 6